

Aerofoil profile modification effects for improved performance of a vertical axis wind turbine blade

by

Md. Farhad Ismail

B.Sc., Bangladesh University of Engineering and Technology, 2012

Thesis Submitted in Partial Fulfillment of the
Requirements for the Degree of
Master of Applied Science

in the
School of Mechatronic Systems Engineering
Faculty of Applied Science

© Md. Farhad Ismail 2014

SIMON FRASER UNIVERSITY

Fall 2014

All rights reserved.

However, in accordance with the *Copyright Act of Canada*, this work may be reproduced, without authorization, under the conditions for "Fair Dealing." Therefore, limited reproduction of this work for the purposes of private study, research, criticism, review and news reporting is likely to be in accordance with the law, particularly if cited appropriately.

Approval

Name: Md. Farhad Ismail
Degree: Master of Applied Science
Title: *Aerofoil profile modification effects for improved performance of a vertical axis wind turbine blade*
Examining Committee: Chair: Dr. Gary Wang
Professor

Dr. Krishna Vijayaraghavan
Senior Supervisor
Assistant Professor

Dr. Siamak Arzanpour
Supervisor
Associate Professor

Dr. Jason Wang
Internal Examiner
Assistant Professor

Date Defended/Approved: October 16, 2014

Partial Copyright Licence



The author, whose copyright is declared on the title page of this work, has granted to Simon Fraser University the non-exclusive, royalty-free right to include a digital copy of this thesis, project or extended essay[s] and associated supplemental files (“Work”) (title[s] below) in Summit, the Institutional Research Repository at SFU. SFU may also make copies of the Work for purposes of a scholarly or research nature; for users of the SFU Library; or in response to a request from another library, or educational institution, on SFU’s own behalf or for one of its users. Distribution may be in any form.

The author has further agreed that SFU may keep more than one copy of the Work for purposes of back-up and security; and that SFU may, without changing the content, translate, if technically possible, the Work to any medium or format for the purpose of preserving the Work and facilitating the exercise of SFU’s rights under this licence.

It is understood that copying, publication, or public performance of the Work for commercial purposes shall not be allowed without the author’s written permission.

While granting the above uses to SFU, the author retains copyright ownership and moral rights in the Work, and may deal with the copyright in the Work in any way consistent with the terms of this licence, including the right to change the Work for subsequent purposes, including editing and publishing the Work in whole or in part, and licensing the content to other parties as the author may desire.

The author represents and warrants that he/she has the right to grant the rights contained in this licence and that the Work does not, to the best of the author’s knowledge, infringe upon anyone’s copyright. The author has obtained written copyright permission, where required, for the use of any third-party copyrighted material contained in the Work. The author represents and warrants that the Work is his/her own original work and that he/she has not previously assigned or relinquished the rights conferred in this licence.

Simon Fraser University Library
Burnaby, British Columbia, Canada

revised Fall 2013

Abstract

Due to the growing need of sustainable energy technologies, wind energy is gaining more popularity day by day. For micro power generation vertical axis wind turbine (VAWT) is preferred due to its simplicity and easy to install characteristics. This study investigates the effects of profile-modification on a NACA0015 aerofoil used in VAWTs. The profile-modifications being investigated consist of a combination of inward semi-circular dimple and Gurney flap at the lower surface of the aerofoil. The study also uses a Response Surface Analysis (RSA) based fully automated optimization technique to maximize the average torque produced by the wind turbine blade. The data set used in the RSA optimization is generated using computational fluid dynamics (CFD) simulations. In order to ensure reliability, the model used in the CFD simulations is validated against previous experimental results. The optimized shape of the modified aerofoil is shown to improve in the aerodynamics of the wind turbine blade under both static and dynamic conditions.

Keywords: NACA 0015 aerofoil; Vertical axis wind turbine (VAWT); Shape optimization; Response surface analysis (RSA); Dynamic condition.

Acknowledgements

I would like to express my immense gratitude to my supervisor Dr. Krishna Vijayaraghavan for his guidance, careful support, constant encouragement and endless patience during the course of this research. His academic experience, professional attitude and positive personality have always inspired me. His confidence in me is also a great source of motivation during my research work. I would also like to thank Dr. Siamak Arzanpour and Dr. Jason Wang for kindly reviewing my thesis. I would like to extend my gratefulness to Dr. Gary Wang for his time and energy as my session defense chair.

I would like to thank Professor Gary Wang as I have learned a lot of things from his optimization course. Over the last two years, I have benefited greatly from the support of my friends. Particularly, I would like to thank Mr. Masum, Mr. Ramin and Mr. Mehdi for their encouragement and support. I express my deepest gratitude to all of my family members who have always encouraged and supported me throughout my academic journey. More specifically, I owe a debt of gratitude to my parents who have sacrificed a lot and put aside their comforts for the sake of my better education.

Table of Contents

Approval.....	ii
Partial Copyright Licence	iii
Abstract.....	iv
Acknowledgements	v
Table of Contents.....	vi
List of Tables.....	viii
List of Figures.....	ix
Nomenclature.....	xii
Chapter 1. Introduction	1
1.1. Literature Review.....	3
1.1.1. Shape of wind turbine blades.....	5
1.1.2. Aerofoil profile modification.....	6
1.2. Design and Optimization.....	8
1.2.1. Turbulence Flow modelling.....	9
1.2.2. Summary	10
1.3. Thesis Outline	12
Chapter 2. Numerical model development.....	13
2.1. Average torque.....	13
2.2. CFD Modelling Technique and Governing equations.....	15
2.3. Computational domain and boundary conditions	20
2.4. Aerofoil geometry	21
2.5. Mesh independency test and model validation	21
2.6. Results and discussions	23
Chapter 3. Optimization study	27
3.1. Optimization method.....	27
3.2. CFD and optimization	28
3.3. Optimization procedure for this study.....	28
3.4. Optimization results	32
Chapter 4. Parametric study: Dynamic condition analysis.....	44
4.1. Problem statement	45
4.2. Numerical techniques and method of analysis.....	46
4.3. Validation studies for the dynamic case.....	49
4.4. Performance of NACA 0015 aerofoil under pitching oscillation	51
4.5. Performance comparison between the standard NACA 0015 and the optimized aerofoil	60

Chapter 5. Conclusions and Future Work.....	70
References	72

List of Tables

Table 3.1 Response results of selected experimental data sets	32
Table 3.2 ANOVA results	33
Table 3.3 RSA Result.....	33
Table 3.4 Optimized Value	33
Table 4.1 Performance comparison between NACA 0015 and optimized aerofoil	69

List of Figures

Figure 1.1.	Wind turbine classifications: (a) horizontal axis [4] and (b) vertical axis [5] wind turbine.	2
Figure 1.2.	Lift coefficient at different angle of attack for NACA 0012 aerofoil [9].....	4
Figure 1.3	Gurney flap on the trailing edge of the aerofoil.	7
Figure 1.4	Dimple on the surface of the aerofoil.	8
Figure 2.1.	Force analysis of a vertical axis wind turbine.....	15
Figure 2.2.	Computational domain (wall function) starts with a distance 'y' from the solid wall [24].....	17
Figure 2.3.	Computational domain having the aerofoil.....	20
Figure 2.4.	Computational domain showing the boundary conditions (not in scale).	20
Figure 2.5.	NACA0015 having gurney flap with inward dimple on the lower surface near the trailing edge.	21
Figure 2.6.	Complete mesh view- denser mesh at the circular pseudo sub domain near the aerofoil.....	22
Figure 2.7.	Boundary layer mesh near the aerofoil surface.	22
Figure 2.8.	Simulation validation and mesh independency test.	23
Figure 2.9.	Variation of lift coefficient at various angles of attack.....	24
Figure 2.10	. Variation of drag coefficient at various angles of attack.	24
Figure 2.11.	Variation of Lift to drag ratio at various angles of attack.	25
Figure 2.12.	Streamlines (superimposed with velocity contour) for NACA 0015 at 7° angle of attack.....	25
Figure 2.13.	Streamlines (superimposed with velocity contour) for NACA 0015 having inward dimple at 7° angle of attack.	25
Figure 2.14.	Streamlines (superimposed with velocity contour) for NACA 0015 having dimples and flaps at 7° angle of attack.....	26
Figure 3.1	. Flow chart of the optimization process.	31
Figure 3.2.	Optimization (maximization) history for Genetic algorithm: force coefficient values at different iteration (generation).	34
Figure 3.3.	Optimization (maximization) history for Simulated Annealing algorithm: force coefficient values at different iterations.	35
Figure 3.4.	Tangential Force Variation at different azimuthal angle.	35
Figure 3.5.	Variation of lift coefficient at different azimuthal angle.	36

Figure 3.6.	Velocity contour superimposed with flow streamlines for NACA 0015 at various azimuthal angles.	39
Figure 3.7.	Velocity contour superimposed with flow streamlines for the optimized aerofoil at various azimuthal angles.	43
Figure 3.8.	Flow separation (superimposed with velocity contour) near the trailing edge for the (a) standard NACA 0015 and (b) optimized aerofoil at azimuthal angle, $\theta = 60^\circ$	43
Figure 4.1.	Angle of attack as a function of azimuthal angle at different tip speed ratios.	44
Figure 4.2.	Simple schematic of the aerofoil pitching motion.	46
Figure 4.3.	Sinusoidal free stream (inlet) velocity (a) Horizontal and (b) Vertical velocity field.	47
Figure 4.4.	Comparison of lift coefficient between previously published experimental study [23], [59] and current numerical simulation at $Re_c = 1.35 \times 10^5$ for oscillating motion: (a) $7.5^\circ \sin(18.67t)$; (b) $15^\circ \sin(18.67t)$	51
Figure 4.5.	Tangential Force Coefficient at different (a) revolution and (b) azimuthal Angle for the condition $7.5^\circ \sin(18.67t)$	53
Figure 4.6.	Tangential Force Coefficient at different (a) revolution and (b) Azimuthal Angle for the condition $7.5^\circ \sin(41.89t)$	54
Figure 4.7.	Tangential Force Coefficient at different (a) revolution and (b) azimuthal Angle for the condition $16.6^\circ \sin(18.67t)$	55
Figure 4.8.	Tangential Force Coefficient at different (a) revolution and (b) azimuthal Angle for the condition $16.6^\circ \sin(41.89t)$	56
Figure 4.9.	Streamlines around the aerofoil surface for the oscillating motion (a)-(e): $16.6^\circ \sin(18.67t)$ and (f)-(g): $16.6^\circ \sin(41.89t)$	60
Figure 4.10.	Velocity contours (single blade) superimposed with the streamlines for for the oscillating motion $8^\circ + 10.6^\circ \sin(18.67t)$ at different angles of attack at $Re_c = 3.6 \times 10^5$: (a)-(c) NACA 0015 and (d)-(f) optimized aerofoil.	63
Figure 4.11.	Tangential force comparison (single blade) between NACA 0015 and optimized aerofoil at $Re_c = 3.6 \times 10^5$ for oscillating motion: $8^\circ + 10.6^\circ \sin(18.67t)$	64
Figure 4.12.	Tangential force comparison (single blade) between NACA 0015 and optimized aerofoil at $Re_c = 2.35 \times 10^5$ for oscillating motion: $8^\circ + 10.6^\circ \sin(18.67t)$	64
Figure 4.13.	Velocity contours (m/s) superimposed with the streamlines for the oscillating motion $5^\circ + 16.6^\circ \sin(18.67t)$ at $Re_c = 2.35 \times 10^5$: (a)-(b) NACA 0015 and (c)-(d) optimized aerofoil (double blade).	66

Figure 4.14.	Tangential force comparison (double blade) between NACA 0015 and optimized aerofoil at $Re_c = 2.35 \times 10^5$ for oscillating motion: $8^\circ + 10.6^\circ \sin(18.67t)$	67
Figure 4.15.	Tangential force comparison (single blade) between NACA 0015 and optimized aerofoil at $Re_c = 2.35 \times 10^5$ for oscillating motion: $5^\circ + 16.6^\circ \sin(18.67t)$	67
Figure 4.16.	Tangential force comparison (double blade) between NACA 0015 and optimized aerofoil at $Re_c = 2.35 \times 10^5$ for oscillating motion: $5^\circ + 16.6^\circ \sin(18.67t)$	68

Nomenclature

C	Chord length (m)
C_D	Drag force coefficient
C_L	Lift force coefficient
C_T	Tangential force coefficient
f	Pitching frequency (Hz)
F_D	Drag force (N)
F_L	Lift force (N)
F_T	Average tangential force (N)
k	Reduced frequency
Re_c	Chord Reynolds number
U	Wind Velocity (m/s)
U_∞	Free stream wind velocity (m/s)
α	Local angle of attack, AOA (deg.)
θ	Azimuthal angle (deg.)
ω	Angular speed (rad/s)

Chapter 1.

Introduction

It is estimated that there approximately 10 million megawatts power are at any one time available in the earth's atmosphere because of wind energy [1]. Energy extraction from wind energy is rapidly competitive to power production from other sources like coal [1]. Currently 0.55% of the world electricity generation is produced by wind energy [1] and better wind turbine design can aid in the increased adoption of wind power.

Wind turbines convert kinetic wind energy to electricity with the aid of a generator. Wind turbines are classified into horizontal axis wind turbine (HAWT) and the vertical axis wind turbine (VAWT) based on their axis of rotation (Figure 1.1). In the case of HAWTs, blades rotate around the axis which is parallel to the flow while VAWT rotates around the axis which is perpendicular to the flow direction. HAWT are better suited for large scale energy generation while VAWT are omni-directional and better suited for small-scale micro power generation [2]. VAWTs are quiet and easy to install as well as easy to manufacture, and can take wind from any direction [3].



(a)



(b)

Figure 1.1. Wind turbine classifications: (a) horizontal axis [4] and (b) vertical axis [5] wind turbine.

Due to the continuous rise of energy demand and limited amount of conventional energy sources, now-a-days focus has been given to extract more energy from environmentally friendly alternative energy sources, such as wind. For simple design and low installation cost VAWTs are gaining more popularity [3]. In the areas where wind flow patterns are very irregular and flow direction changes quickly in a frequent matter i.e. lower elevation or urban areas, VAWTs are better suited for installation. Thus the motivation of the present study is to maximize the performance of a VAWT blade for micro power generation.

VAWTs are sub-classified into Darrieus rotor and Savonius rotor wind turbines [3]. Darrieus rotor wind turbines make use of the lift produced by the blades while Savonius rotor turbines produce power due to the drag created by the blades. In this study the focus has been given to improve the performance of Darrieus VAWTs. As VAWTs rotate about an axis perpendicular to the flow, the angle of attack (orientation of the blade relative to the wind flow) is not constant and the blades oscillate relative to the wind-direction. Hence the average torque should be used as the metric while comparing the performance of VAWTs. The calculation of this average torque is discussed in section 2.1. One of the most commonly used methods in VAWT research is the classical

Blade Element Momentum theory (BEM) introduced by Glauert (1926). The theory is basically based on the calculation of flow velocity through the VAWT by equating the upstream and downstream pressures on the blades with the rate of change of momentum of the fluid. The flow is assumed to be steady and incompressible.

1.1. Literature Review

The efficiency of wind turbines is primarily dependent on the design of the profile of the turbine blade. Thus, aerofoil design, modification and performance optimization for wind turbine application are the active fields of research. To increase the performance of the available turbine blades, one approach is to apply active or passive flow control features on the aerofoil surface. Passive flow control techniques include installing vortex generators and gurney flaps (refer to section 1.1.2) to the trailing edge of blades [4, 5]. These types of flow control techniques or modifications provide increased lift coefficient which ultimately increases the tangential force. Due to fluid-structure interaction, laminar to turbulent transition of the boundary layer can occur nearly to the leading edge. To avoid the premature transition, aerofoils can be equipped with a blunt trailing edge [8].

Due to the complexity of the unsteady flow conditions of the VAWT blades, Computational Fluid Dynamics (CFD) becomes a popular way to analyze the aerodynamic performance. CFD technique was applied by various researchers to calculate the turbulent flow separation and wake generation around the VAWT blades. In CFD models, a physical flow field can be represented by applying the conservation of mass, momentum and energy equations (for compressible flows). The flow field is then divided (discretized) into specific number of cells which are called grids. Then the equations are solved at discrete grid points at each time step by applying various discretization schemes. By solving the governing equations at these discrete grid points, the flow field can be obtained around the VAWT blades. The solution can be used to obtain the values of specific interest (e.g. lift, drag, power, moment etc.) which is called post processing. VAWT blades normally use standard aerodynamic shaped wings (aerofoil) developed by the National Advisory Committee for Aeronautics (NACA). Figure 1.2 shows a typical performance of NACA 0012 aerofoil [9]. Angle of attack is the angle between the aerofoil and the wind direction. Beyond a certain AOA (i.e. 10° in the figure),

the lift decreases. This condition is called the stall condition. When the aerofoil operates dynamically (for instance the case of VAWT blade), during downstroke the aerofoil goes through the wake generated on its upstroke. For this reason, stall conditions for steady state static conditions and dynamic conditions are different (refer to Chapter 4).

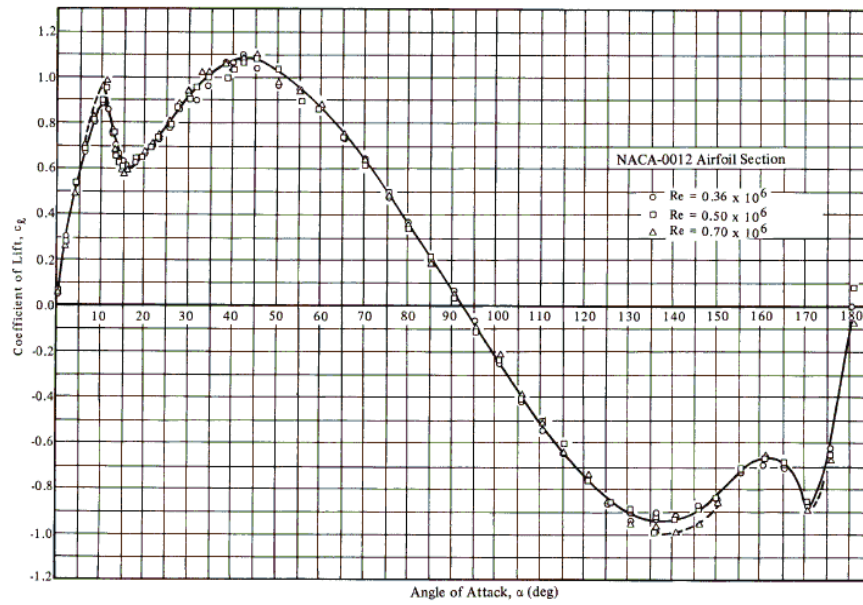


Figure 1.2. Lift coefficient at different angle of attack for NACA 0012 aerofoil [9].

Sheldahl et al. [9] reported experimental investigations of the aerodynamic characteristics of NACA 0012, NACA 0015, NACA 0018 and NACA 0021 aerofoils for use in VAWT. Guerri [10] et al. numerically investigated the aerodynamic performance of a small VAWT blade [11]. The results showed that CFD methods gave a good prediction of VAWT blades aerodynamic performance. Ferreira et al. [12], [13] simulated the dynamic stall of VAWT blades by CFD techniques and used different types of turbulent models [11] to validate their experimental results i.e. Reynolds-averaged Navier–Stokes (RANS) simulation, Large eddy simulation (LES) and Detached eddy simulation (DES) [14]. As RANS turbulence models need less computational resources and time, these models are very much popular for predicting the flow turbulence around the VAWT blades. RANS turbulence models can be classified into three parts [11] : Linear eddy viscosity models, Nonlinear eddy viscosity models and Reynolds stress model (RSM). Among them, linear eddy viscosity models are most commonly used for wind turbine research. Linear eddy viscosity models can again be divided into different parts:

Algebraic models, one-equation model and two equation model. But two most popular models are the One equation (e.g. Spalart-Allmaras model) and Two equations models (e.g. $k-\epsilon$ models, $k-\omega$ models). These models [11], [14] are modified for specific applications based on the low and high Reynolds number applications (refer to 2.1). For low Reynolds number applications (specifically for VAWT blade simulation) Spalart-Allmaras model, RNG $k-\epsilon$ model, Realizable $k-\epsilon$, Wilcox's $k-\omega$ model and SST $k-\omega$ models are commonly used [2], [3], [10], [12], [13], [15]–[20]. Hamada et al. [21] applied RNG $k-\epsilon$ turbulence model to analyze the performance of VAWT blades. The results showed that the torque reached the minimum value at an azimuthal angle of 13 degree and the maximum value at 90 degree. Wang et al. [22] applied standard $k-\omega$ and SST $k-\omega$ models [11], [14] and tried to validate the results of Lee et al. [23] for wind turbine applications under deep dynamic stall conditions (refer to Chapter 4). The aerodynamic performance of wind turbine aerofoil under dynamic flow condition has been investigated by Gharali et al. [16] and Ahmadi et al. [15]. From their study it is seen that the tangential force value is much higher for the dynamic cases than that of the static case. Gharali et al. [16] have used SST $k-\omega$ and Realizable $k-\epsilon$ turbulence models. But no researchers have found a proper turbulence model to predict the VAWT blade performance accurately. Thus VAWT blade simulations for low Reynolds number applications are still an active area of research. Finite element based package COMSOL Multiphysics [24] has provided another turbulence model termed as 'Revised $k-\omega$ turbulence model' which is actually the modified version of the Standard $k-\omega$ turbulence model [14]. This model has not yet been tested for VAWT blade simulation under dynamic conditions. Thus, in this study this turbulence model is used to validate the experimental results for pitching oscillation cases (refer to Chapter 4). After getting reasonable accuracy to predict the flow parameters under light dynamic stall cases, further simulation has been carried out to analyze the performances of VAWT blades.

1.1.1. Shape of wind turbine blades

VAWT blade shape is very essential to extract the maximum possible amount of energy from the wind. Cross sections of Darrieus VAWT blades normally use standard aerodynamic shaped wings (aerofoil) developed by the National Advisory Committee for Aeronautics (NACA). These aerofoils are developed specifically for high velocity flow

conditions applicable for aircrafts. These types of aerofoils have larger value of lift-to-drag ratio, which is a key parameter for keeping the aircraft engine with minimum fuel consumption. But the lift-to-drag ratio has less meaning on VAWT blades (refer to section 2.1). Moreover, aircraft aerofoil experiences almost constant angle of attack. For the case of a VAWT blade the angle of attack changes frequently in a cyclic manner for which the direction of the forces acting on the aerofoil changes significantly (refer to section 4.1). All of these aerofoils face stall conditions after a certain value of angle of attack (AOA). In aerofoil aerodynamics, stall condition is the reduction in the lift force generated by the aerofoil as further increase of the angle of attacks. This happens when the critical AOA of the aerofoil is exceeded. This point is normally larger for the unsteady dynamic condition than the steady state static conditions [23]. For this reasons NACA aerofoils should be checked whether they are suited to use on VAWT blades. Various researchers have tested various shaped aerofoil for VAWT applications and among them NACA 0012 and NACA 0015 are most commonly used for this specific application [2], [22]. In the present study some modifications are made to the standard NACA 0015 aerofoil in hopes to increase the wind turbine performance.

1.1.2. Aerofoil profile modification

Researchers working on aerofoil for non-VAWT application have proposed two profile modifications that have been independently shown to enhance aerofoil aerodynamics. The first modification is a vertical flap known as Gurney flap (Figure 1.3). Gurney flap (GF) is named after the race car driver Dan Gurney [25]. He first used this type of modification to increase the downward force which ultimately increases the speed of the car significantly. GF is simply a short flat plate attached to the pressure side trailing edge of the aerofoil. Gurney flaps have been experimentally shown to improve the lift coefficient of the aerofoil [26]. Gurney flap of height 1.25% of chord length (C) increases the lift with only a small increase in drag coefficient [26]. The drag coefficient is known to rise rapidly for flap sizes larger than 2%- C . This phenomenon is explained in studies on NACA 0012 [27], NACA 0011 [28] and LA 203A [29] aerofoils which note that the Gurney flap increases the suction of the aerofoil upper surface and pressure on the lower surface which in turn result in increased lift. Similar trends in lift and drag coefficients have been observed in other aerofoil such as race car wings [30], [31].

Gurney flap having different configurations has been investigated to improve the aerodynamics of aerofoil. Saw-toothed GF [7], [23], [27], [32]–[34], [35], and/or perforated GF [36] can be the modifications which in turn improves the performance of aerofoil. Such configurations moved the separation point forward over the suction surface of the aerofoil with increasing the lift to drag ratio as compared to a regular GF of same shape. Wang et al. [33], [37] introduced a combination of the Gurney flap with trailing edge flap which increase the lift coupled with a decrease in lift-to-drag performance [38]. To understand the mechanism of such passive flow control techniques various experimental studies [28], [39]–[41] have also been performed by many researchers. From these studies it has been seen that due to the presence of GF, a pair of counter-rotating vortices arise at downstream of the trailing edge which in turn decrease the adverse pressure gradient [25], [26], [33], [37]. Thus the flow separation delays over the suction or upper surface of the aerofoil. The vortices also increase the velocity of the fluid on the upper surface, which in turn increase the lift.



Figure 1.3 Gurney flap on the trailing edge of the aerofoil.

Dimples on the surface of the aerofoil, the second modification, can act as a vortex generator to improve the lift coefficient of aerofoil [42]. These dimples increase flow turbulence and reduce the wake and thereby reducing the drag coefficient. They help increase the overall lift at a higher angle of attack. From the literature review study it is seen that though some research works has been carried out using the outward dimple for improving the aerofoil performance [42] but to the best of author's knowledge no research work has been done using the inward dimple on the aerofoil surfaces. This has been shown to delay the angle of the stall.

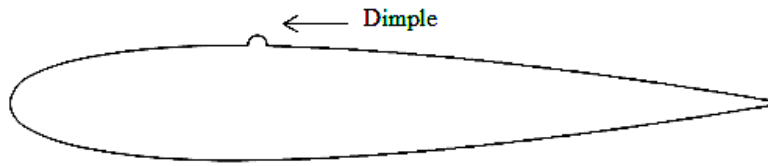


Figure 1.4 Dimple on the surface of the aerofoil.

1.2. Design and Optimization

Aerofoil aerodynamics can be classified as two groups: the design and the analysis problems. Analysis problems may also refer to as direct problems; the flow field details can be obtained when the aerofoil geometry is specified. For the design based problems which also may refer to as inverse problems, the aerofoil geometry can be generated by fixing the flow fields features, such as the pressure or velocity distributions on the aerofoil surfaces. The design approach occasionally yields impractical aerofoil geometry [41]. On the other hand, the analysis of the flows around specific aerofoil profile can always arrive at a meaningful result. Numerical optimization using gradient-based methods (GBMs) has been used in conjunction with flow analysis to design aerofoil profile [43]. However GBMs have some drawbacks [44]. The optimal point search often leads to a local minimum and the efficiency of the GBM based optimization process depends on the method adopted to compute the gradient of objective and constraint functions. Additionally gradient based evaluation sometimes becomes highly sensitive due to the presence of noises or existence of many local minima's in the objective/constraint functions.

Fluid flow analysis can also be applied with response surface methods (RSM). Details on RSM can be found in [45]. RSM-based optimization shows a good number of advantages [44], [46]. RSM consists of generation of objective function by numerical simulations or experiments and the construction of a reliable response surface model through a regression analysis. The response surface is then optimized. The response surface is often assumed to be a second-order polynomial function which can smooth out the high-frequency noise of the original objective function and is expected to

approximate a solution near the global optimum [47]. This ultimately reduces computational time and cost. Due to these advantages, RSM based optimization has been widely applied to single- and multi-objective optimization problems [19], [20], [45], [47]–[51].

1.2.1. Turbulence Flow modelling

The cyclic variation of the angle of attack of a vertical axis wind turbine blade is very similar to the flow around a pitching aerofoil. Flow behaviour around a pitching aerofoil has been investigated previously by various researchers for aviation applications such as McAlister et al. [52], McCroskey et al. [53], Piziali [54] and more recently Tsang et al. [55]. In fluid mechanics the Reynolds number can be defined as the ratio of the inertia and the viscous force. After a certain value of Reynolds number (i.e. $Re > 10^5$) the flow becomes too unstable and non-uniform which can be defined as turbulent flow condition. Reynolds number value upto 10^6 can be defined as low Reynolds number turbulent flow where the viscous force has significant effects on the flow conditions. Sections 2.1 and 4.2 will give detail description of the turbulent flow cases. Following the experimental work on pitching aerofoils, a wide range of turbulence models were applied. Though the obtained numerical results could not capture the flow behaviour accurately but satisfactory results were obtained using the Shear Stress Transport (SST) $k-\omega$ model of Menter [56], [57]. In this study, the revised $k-\omega$ turbulence model [24], [58] has been considered for the unsteady light dynamic stall conditions for VAWT blade applications. This model has been considered to model the flow turbulence for the oscillating dynamic condition for the following reasons:

Under dynamic conditions, the stall is delayed in comparison to the static conditions. In experimental studies, deep dynamic stall is observed to occur at a higher angle $\gtrsim 20^\circ$ compared to static stall which is observed at angle of attack $\gtrsim 12^\circ$ [35]. Under dynamic conditions, almost attached flow has been observed even at an angle of attack of 18° . The oscillating motion occurred at an angle of attack larger than the static stall and smaller than the dynamic stall cases is known as the light dynamic stall cases [59]. It is noted in previous literature that the flow parameters are too much sensitive to the oscillating frequency values for dynamic stall conditions [15], [22], [23], [60].

Turbulence modeling under dynamic and pitching oscillation condition is still an active area of research and no current turbulence model can accurately captures the flow behaviour of an aerofoil under dynamic oscillation conditions [15], [22], [23], [60]. Thus, turbulence models specifically applicable for low Reynolds number cases i.e. RNG k- ϵ , Standard k- ω or SST k- ω , does not result in higher accuracy [15], [22], [23], [60]. Moreover, all of these models are too much sensitive to the input parameters [15], [22], [23], [60]. Recently, the standard k- ω turbulence model has been improved [24], [58] and is developed for low Reynolds number and specifically for light dynamic stall applications but has not been yet validated against the experimental results of pitching oscillation cases. Initial simulations (refer to Chapter 2 and Chapter 4) also revealed SST k- ω to require a huge amount of computation time than the revised k- ω models. It is because revised k- ω turbulence model uses wall function which is computationally more efficient than the SST k- ω model. Detail description of the turbulence models can be found in the Section 2.2 and Section 4.2.

1.2.2. Summary

This study aims to provide a systematic approach to optimizing the blades used in VAWT by studying a NACA 0015 VAWT blade with both inward dimples and a Gurney flaps at the pressure side (lower) surface of the blade near the trailing edge. As the angle of attack of the blades in a VAWT changes continuously even when the wind-speed and rotation speed remains constant (refer to Chapter 3), the study aims to maximize the effective torque rather than to maximize the lift coefficient at a single angle of attack.

From the literature review study, it is found that most of the previous works used standard NACA aerofoils [2], [9], [10], [12], [13], [15], [17], [19], [21], [34], [60]–[63], [64] to investigate the performance of a VAWT blade. In this study, some modifications of the regular NACA aerofoil have been tested and the performance of the modified aerofoils has been compared with the base NACA aerofoil (refer to Chapter 2). It is also found that the value of the forces exerted from the VAWT blades are very much sensitive to the dynamic oscillating conditions [23], [59] e.g. the values of the forces change significantly with the angular velocity, turbulent intensity, wind velocity, oscillating

amplitude etc. For this reason, the optimization study has been carried out under steady state static conditions (refer to Chapter 3) and then the optimized aerofoil has been tested under different dynamic oscillating conditions (refer to Chapter 4). Moreover, most of the previous VAWT optimization research used lift forces or lift to drag ratios as an objective (cost) function to maximize the aerodynamic performance [19], [20], [34]. The study will use a Response Surface Analysis (RSA) based optimization technique which involves evaluating the objective function (in this case calculating the average torque) at discrete points in the parameter space to generate a “response surface”. The optimal distribution of the evaluation points can be achieved using design of experiment (DOE) analysis [45], [47]. To ensure reliability, the CFD models used in this study are validated against the corresponding experimental results published in the literature.

To the best of the author knowledge, the present study is the first attempt to investigate the simultaneous effects of Gurney flap and dimple configuration as well as to apply RSA based optimization method to maximize the aerodynamic performance of VAWT blade.

Thus, the main objectives of this research can be summarized as:

- (a) To introduce new surface modification features i.e. Gurney flap and inward dimple at the trailing edge of the aerofoil.
- (b) To compare and improve the performance of VAWT blades with respect to the standard NACA 0015 aerofoil.
- (c) To find an optimized arrangement of this modification for maximum power generation under steady state condition.
- (d) To test (validate) the revised $k-\omega$ turbulence model whether it can be applicable for VAWT applications under light dynamic stalls (refer to Chapter 4).

- (e) To analyze the performance of the obtained optimized aerofoil profile under unsteady dynamic condition for single and double bladed wind turbine applications.

1.3. Thesis Outline

Chapter 1 includes an introduction including a literature review study on wind turbines and related optimization research. The computational procedure and validation study are presented in Chapter 2. Results of the initial study of the surface modifications are also presented in this chapter. Chapter 3 describes the optimization study to maximize the wind turbine output power under steady state condition. Performance of the optimized aerofoil (single and double bladed case) under dynamic oscillating pitching condition is presented in Chapter 4. Conclusions and recommendations regarding future work are included in Chapter 5.

Chapter 2.

Numerical model development

This chapter describes the CFD modelling and validation approach employed in the optimization process. Many turbulence models are available for predicting the flow parameters at both low and high ($\geq 10^6$) Reynolds number flow. After completing the literature review study, it can be determined that a two-dimensional *Reynolds-Averaged Navier-Stokes equations* (RANS) based turbulent flow equations (refer to section 2.2) is the most promising approach to determine the performance of a VAWT blade under both steady-state and dynamic condition [2], [16], [22]. Detail documentation on turbulence modeling can be found in [11] and [24]. In a two-dimensional analysis, numerical modelling domain limits to a single cross-section of the VAWT blade which in turn minimizes the computational expense. Previous VAWT blade analyses have employed a similar approach in general. However, those are limited to validate the experimental results and to select the appropriate blade profile (airfoil) [2], [12], [15]–[17], [61], [63], [64]. Initially the profile modification effects and the optimization process (refer to Chapter 3) consist of the steady state simulations. Then, the model has been expanded to incorporate the effects of oscillating frequency and amplitude under dynamic condition.

2.1. Average torque

Figure 2.1 shows the aerodynamic forces acted on a wind turbine airfoil. The orientation of the blades relative to the true wind direction is known as the azimuthal angle (θ). As the VAWT rotates, the orientation of the blades relative to the true wind direction (azimuthal angle, θ), changes from 0 to 360°. As a result, the chordal/tangential velocity (V_c) and normal velocity (V_n) can be written as following [3] in terms of wind velocity (U) :

$$V_c = U(\lambda + \cos \theta) \quad (2.1)$$

$$V_n = U \sin \theta \quad (2.2)$$

Where,

$$\lambda = \frac{\omega R}{U_\infty} \text{ is the tip speed ratio.}$$

In the absence of flow restrictors, the induced velocity can be assumed equal to the free-stream velocity, i.e. $U = U_\infty$. The effective wind velocity (W) and the angle of attack (α) are given as:

$$W = \sqrt{V_c^2 + V_n^2} \quad (2.3)$$

$$\alpha = \tan^{-1} \left(\frac{V_n}{V_c} \right) \quad (2.4)$$

For aerofoils, the lift coefficients (C_L) and drag coefficients (C_D) are defined relative to the wind direction. The lift coefficients (C_L) and drag coefficients (C_D) represent the normalized lift and drag force respectively. Hence we define tangential force coefficient C_T to represent the normalized tangential force as

$$C_T = C_L \sin \alpha - C_D \cos \alpha \quad (2.5)$$

and the tangential force per unit width is given by

$$F_T = \frac{1}{2} C_T \rho c W^2 \quad (2.6)$$

Where, ρ is the density of air

c is the chordal length

This yields an average tangential force,

$$F_{T,avg} = \frac{1}{2\pi} \int_0^{2\pi} F_T(\theta) d\theta \quad (2.7)$$

The chord Reynolds number can be defined as the following where μ is the viscosity; ρ is the density of the fluid.

$$Re = \frac{\rho U_{\infty} c}{\mu} \quad (2.8)$$

From this analysis, it is clear that tangential force is the main key parameter for the power produced by the vertical wind turbine blade. In this study, the average tangential force will be calculated using the above mentioned numerical integration technique.

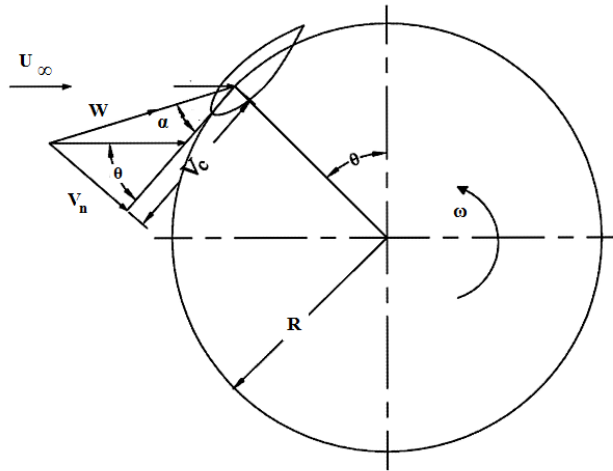


Figure 2.1. Force analysis of a vertical axis wind turbine.

2.2. CFD Modelling Technique and Governing equations

In this study, all the CFD simulation has been performed using the finite element based commercially available software COMSOL Multiphysics [24]. CFD simulations are performed to obtain a better understanding of the velocity and pressure field experienced by the VAWT blade. CFD simulation includes using numerical techniques to solve the flow fields applying different boundary conditions. For the isothermal, incompressible flow field, the Navier-Stokes consists of the equations for

conservation of momentum and conservation of mass (continuity) [11]. Several models exist [65] to model the Reynolds stresses by predicting the turbulent eddy viscosity term to solve the Navier-Stokes equations for turbulent flow condition.

Zero equation models calculate the turbulent eddy viscosity from flow variables i.e. the boundary layer velocity profile. These models do not include convection and diffusion of turbulent energy. This turbulence model is often used for simple flow geometries. A one-equation turbulence model is an improvement on the zero-equation model which solves a turbulent transport equation with a series of model constants to be tuned for the specific flow conditions. The Spalart-Allmaras model [66] is a one-equation model which works well on aerofoils because of its capability to predict the flow separation. The most commonly used models are two-equation models that include the k- ϵ [67], revised k- ω [57] and Shear-Stress Transport (SST) model [58]. The k- ϵ model can predict the turbulence flow field well in free-shear flows, but its predictions of eddy viscosity terms in boundary layer flows and near wall regions are less satisfactory [11], [24]. The k- ω turbulence model can predict the boundary layer flows well at adverse pressure gradient, but it is over sensitive in the highly separated flows. In order to overcome this limitation, a hybrid blend of the k- ϵ and k- ω models, known as the SST model was developed in literature. The model uses a blending function to switch from the k- ϵ to the k- ω model when it approaches a near-wall region. As SST model does not use any wall function, this model is computationally expensive than the standard and revised k- ω turbulence model (refer to Chapter 4). Wall-function simulations normally predict the mesh cells at a certain distance from the solid wall (Figure 2.2). Normally the value of y plus starts at about a distance of 11.06 or larger depending on the Reynolds number [11], [24].

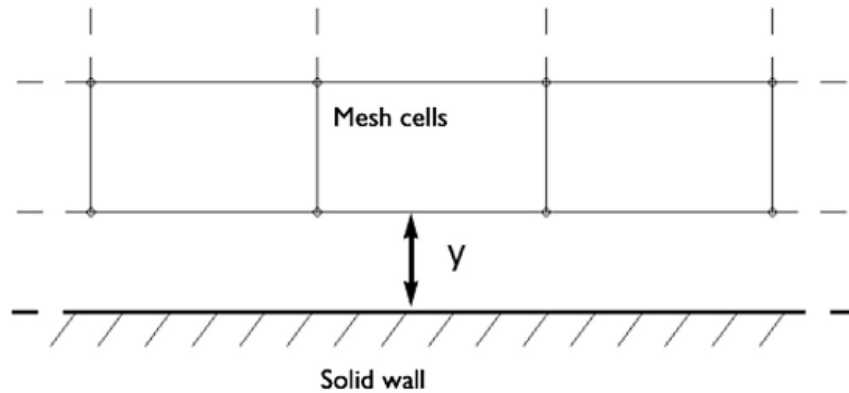


Figure 2.2. Computational domain (wall function) starts with a distance 'y' from the solid wall [24].

The Navier-stokes equations can be expressed as follow [24]:

Continuity equation:

$$\frac{\partial \rho}{\partial t} + \nabla(\rho u) = 0$$

Momentum equation:

$$\rho \frac{\partial u}{\partial t} + \rho (u \cdot \nabla) u = \nabla \cdot [-pI + \tau]$$

Where,

ρ is the density of the fluid,

u is the velocity vector,

p is pressure,

τ is the viscous stress tensor.

The above equations can be solved for specific boundary and initial conditions. For the turbulent flow conditions, the flow parameters fluctuate too much and so to obtain the

mean flow parameters an ensemble of solutions is averaged. This process is known as the Direct Numerical Simulations (DNS) [14]. But obtaining the solutions and ensemble averaging them is computationally very expensive i.e. it needs high computational resources and time. Thus it is more popular to average the equations rather than the solutions. Then for the present simulation the equations for the SST k- ω turbulence model are as follows [11], [24]-

Continuity equation:

$$\rho \nabla \cdot U = 0 \quad (2.9)$$

Reynolds averaged Navier-Stokes (RANS) equation:

$$\rho U \cdot \nabla U + \nabla \cdot (\overline{\rho u' \otimes u'}) = -\nabla p I + \nabla \cdot \mu (\nabla U + (\nabla U)^T) \quad (2.10)$$

Transport equations for k- ω model:

$$\rho \frac{\partial k}{\partial t} + \rho u \cdot \nabla k = P - \rho \beta_0^* k \omega + \nabla \cdot ((\mu + \sigma_k \mu_T) \nabla k) \quad (2.11)$$

$$\rho \frac{\partial \omega}{\partial t} + \rho u \cdot \nabla \omega = \frac{\rho \gamma}{\mu_T} P - \rho \beta \omega^2 + \nabla \cdot ((\mu + \sigma_\omega \mu_T) \nabla \omega) + 2(1 - F_1) \frac{\rho \sigma_{\omega 2}}{\omega} \nabla \omega \cdot \nabla k \quad (2.12)$$

Where,

$$P = \min(P_k, 10 \beta_0^* k \omega)$$

$$\text{And } P_k = \mu_T (\nabla u : (\nabla u + (\nabla u)^T) - \frac{2}{3} (\nabla u)^2) - \frac{2}{3} \rho k \nabla \cdot u$$

The turbulent eddy viscosity is given by,

$$\mu_T = \frac{\rho a_1 k}{\max(a_1 \omega, S F_2)}$$

Here, S is the magnitude of the strain-rate tensor,

$$S = \sqrt{2 S_{ij} S_{ij}}$$

Each of the constants is a blend of the corresponding constants of the k- ϵ and the k- ω model.

$$\phi = F_1 \phi_1 + (1 - F_1) \phi_2 \quad (2.13)$$

The interpolation functions F_1 and F_2 are defined as,

$$F_1 = \tanh(\theta_1^4)$$

$$\theta_1 = \min \left[\max \left(\frac{\sqrt{k}}{\beta_0^* \omega l_w}, \frac{500 \mu}{\rho \omega l_w^2} \right), \frac{4 \rho \sigma_{\omega_2} k}{CD_{k\omega} l_w^2} \right]$$

$$CD_{k\omega} = \max \left(\frac{2 \rho \sigma_{\omega_2}}{\omega} \nabla \omega \cdot \nabla k, 10^{-10} \right)$$

and,

$$F_2 = \tanh(\theta_2^2)$$

$$\theta_2 = \max \left(\frac{2 \sqrt{k}}{\beta_0^* \omega l_w}, \frac{500 \mu}{\rho \omega l_w^2} \right)$$

Where, l_w is the distance to the closest wall. Realizability Constraints are applied to the SST model. From the literature review study the model constants has been obtained by [2], [14], [24],

$$\beta_1 = 0.075, \quad \gamma_1 = 5/9, \quad \sigma_{k1} = 0.85, \quad \sigma_{\omega1} = 0.5$$

$$\beta_2 = 0.0828, \quad \gamma_2 = 0.44, \quad \sigma_{k2} = 1, \quad \sigma_{\omega2} = 0.856$$

$$\beta_0^* = 0.09, \quad a_1 = 0.31$$

2.3. Computational domain and boundary conditions

A sufficiently long domain ($20 \times$ chord length) is chosen to avoid the effects of the outlet condition and resolve the flow behaviour accurately. The aerofoil having a chord length, $c= 0.4$ m chord is located near the center of the domain. To improve the computational efficiency, it is desirable to utilize a circular mesh domain adjacent to the aerofoil surface where the mesh is very fine than away from the aerofoil surface. Hence, two circular sub-domains are defined centered about the aerofoil for this study. The boundary conditions for the two dimensional steady state incompressible fluid flow is similar to the one used by McLaren et al. [2]. Figure 2.1 and Figure 2.4 show the complete flow domain and the boundary conditions respectively. From these figures, it is seen that the downstream length is greater than the upstream length to resolve the turbulence flow parameters well. Triangular meshing is used for the analysis away from the aerofoil surface and the boundary layer mesh is used on the aerofoil surface to predict the flow parameters well. Detail mesh view is shown in the section 2.5.

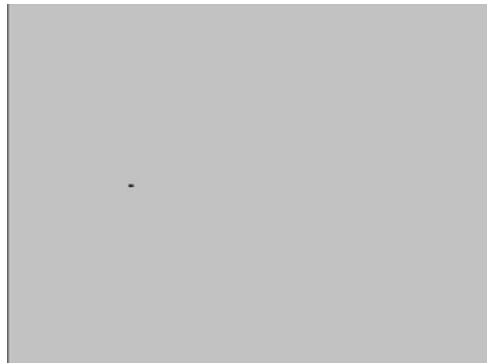


Figure 2.3. Computational domain having the aerofoil.

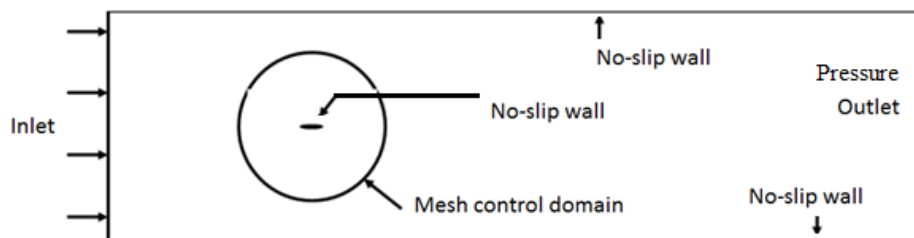


Figure 2.4. Computational domain showing the boundary conditions (not in scale).

The inlet is defined as a velocity inlet while the outlet is set as pressure outlet. The outlet pressure is set 1 atm. No slip wall condition is assumed near the aerofoil surface as well as the upper and lower wall of the domain.

2.4. Aerofoil geometry

In this study, NACA 0015 aerofoil has been used and further modification has been employed for wind turbine performance improvement. The NACA0015 aerofoil having both an inward dimple and a Gurney flap at the lower surface is shown in the Figure 2.5. The aerofoil is analyzed at eleven different angles of attack (ranging from 0° to 22°). The free stream velocity is fixed at 13.45 m/s and the corresponding chordal Reynolds number (Re_c) is 3.61×10^5 . For the initial check and comparison with the standard NACA 0015 aerofoil, Gurney flap height (h) of 1% and the dimple radius (r) of 0.5% of the chord have been taken for the modified one.

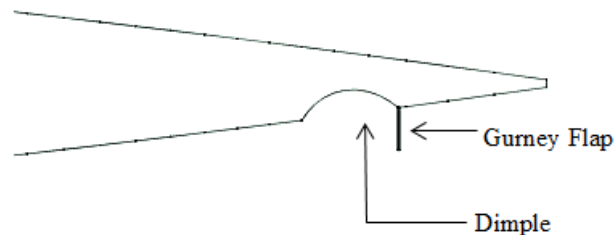


Figure 2.5. NACA0015 having gurney flap with inward dimple on the lower surface near the trailing edge.

2.5. Mesh independency test and model validation

The mesh employed on the flow domain is generated based on a series of mesh independence tests. The boundary layer mesh is governed by the following parameter values: the boundary layer consists of 40 layers with a spreading rate of 1.1. The distance of the first layer from the wall has been taken as the order of $10^{-5} \times c$ [2]. The CFD simulation is validated against previously published experiments for NACA 0015 in Sheldahl et al. [9]. The comparison of lift coefficient in Figure 2.8 shows that the CFD results are within $\pm 5-7\%$ of the experimental results. The error percentage increases with

the angle of attack. This may be attributed to unsteady flow behaviour and boundary layer separation at a higher angle of attack. In this simulation, flow is assumed to be fully turbulent whereas the experimental flow-field is not fully turbulent. To establish mesh independence, the simulations were performed at different mesh counts. From Figure 2.8, it is also seen that a mesh count of approximately 200,000 is sufficient enough to obtain reliable results.

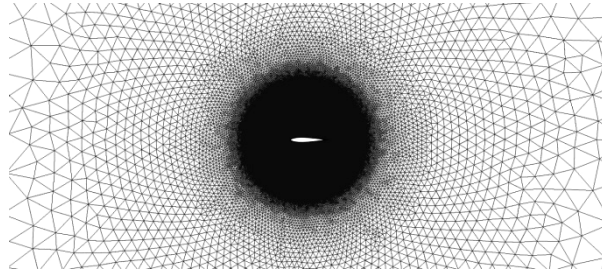


Figure 2.6. Complete mesh view- denser mesh at the circular pseudo sub domain near the aerofoil.

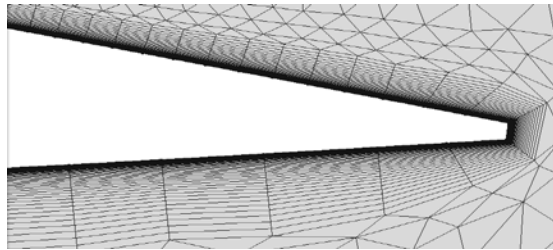


Figure 2.7. Boundary layer mesh near the aerofoil surface.

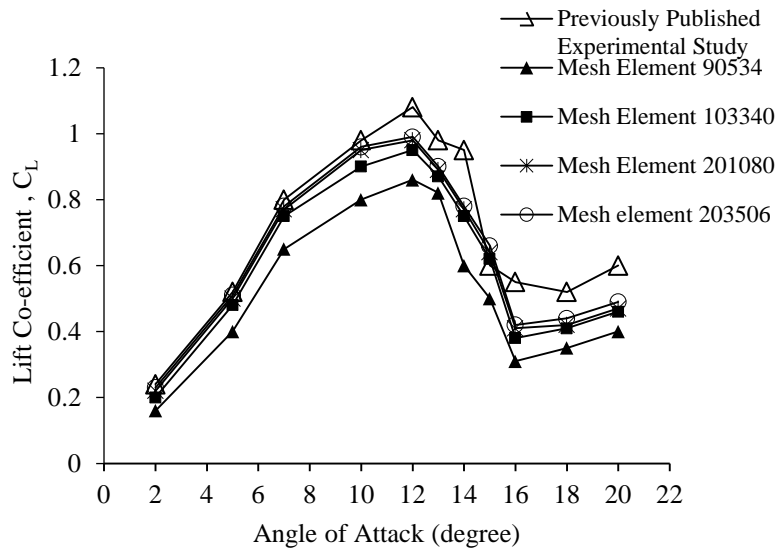


Figure 2.8. Simulation validation and mesh independency test.

2.6. Results and discussions

Dimples and flaps are employed to create turbulence that results in delayed of boundary layer separation. Thus, the stall condition is delayed which in turn increase the tangential force values. Figure 2.9 shows that aerofoil with a combination of dimple and flap has larger lift coefficients than aerofoil with only dimples. Aerofoil with only dimple in turn has larger lift coefficients than the regular NACA 0015 aerofoil. From Figure 2.10 it is seen that aerofoil having dimple and flap shows higher drag coefficient value than the other aerofoil. Figure 2.11 shows that the value of lift to drag ratio increases with increase of angle of attack up to an angle of 7° .

For the case of modified aerofoil having dimples and flaps, turbulence generation is higher than the other aerofoils due to greater flow separation and recirculation (Figure 2.14). Figure 2.12 to Figure 2.14 show the stream lines superimposed with velocity contour the at angle of attack 7° . From the figures it is shown that due to dimples and flap, larger flow recirculation (larger blue region) are generated near the pressure side trailing edge which is the reason of higher lift to drag ratio value than the regular (standard) NACA 0015 aerofoil.

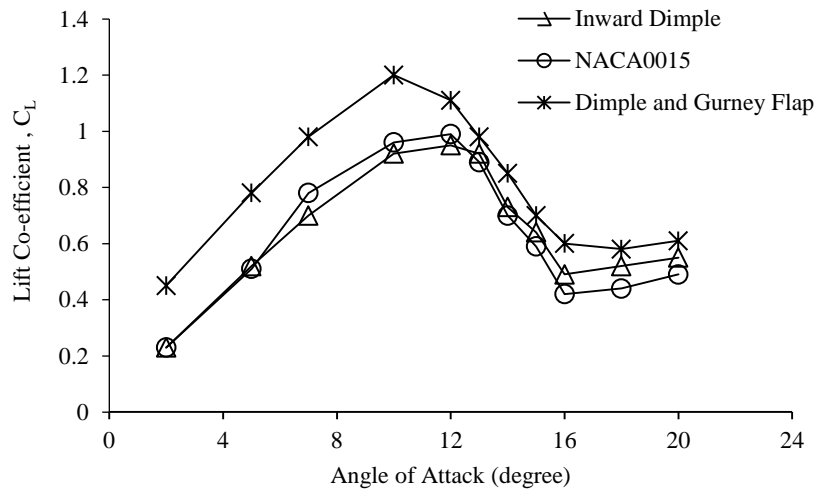


Figure 2.9. Variation of lift coefficient at various angles of attack.

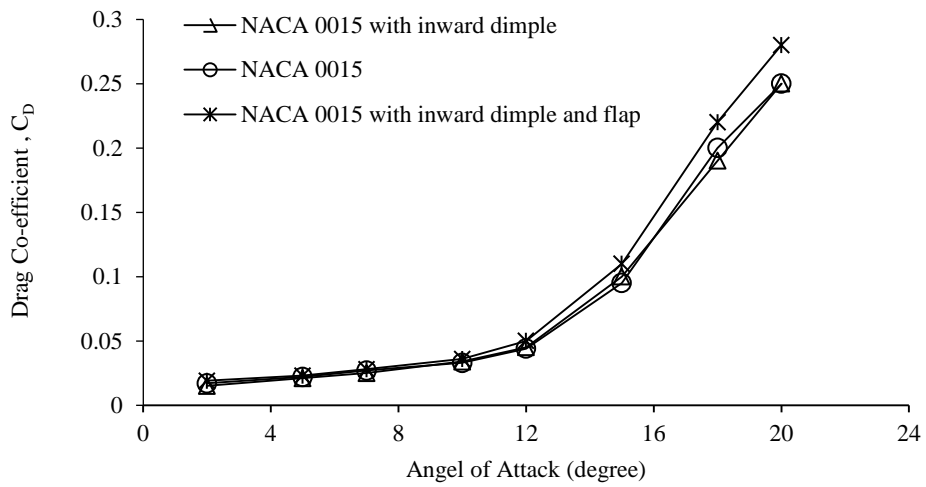


Figure 2.10 . Variation of drag coefficient at various angles of attack.

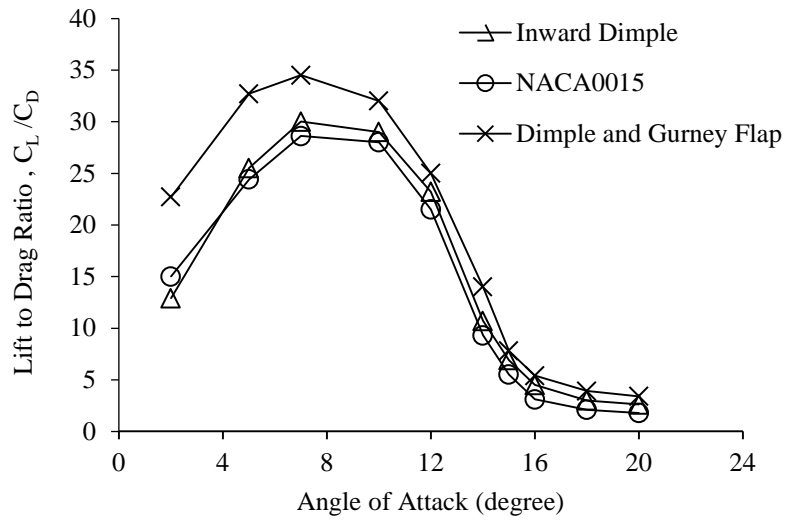


Figure 2.11. Variation of Lift to drag ratio at various angles of attack.

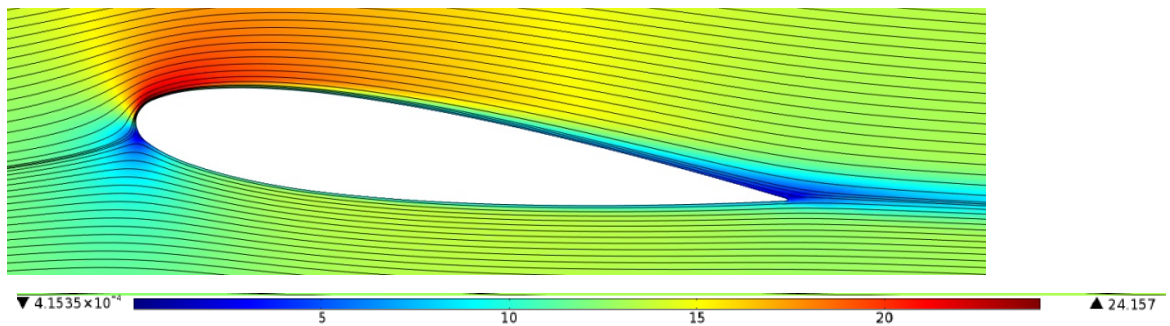


Figure 2.12. Streamlines (superimposed with velocity contour) for NACA 0015 at 7° angle of attack.

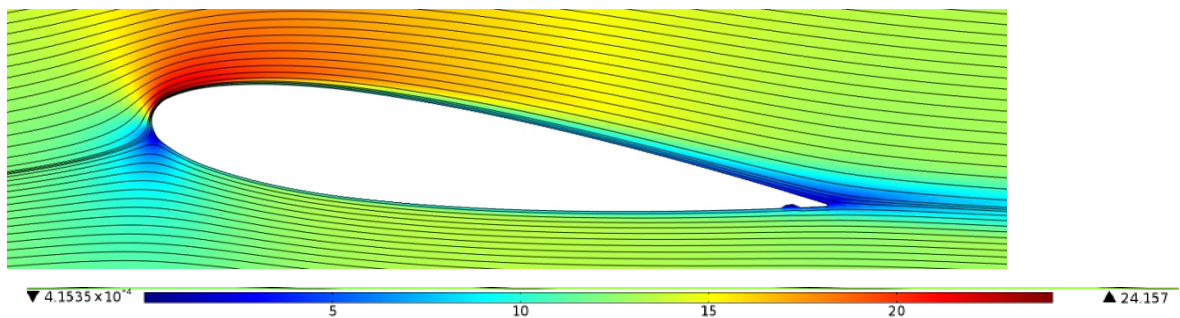


Figure 2.13. Streamlines (superimposed with velocity contour) for NACA 0015 having inward dimple at 7° angle of attack.

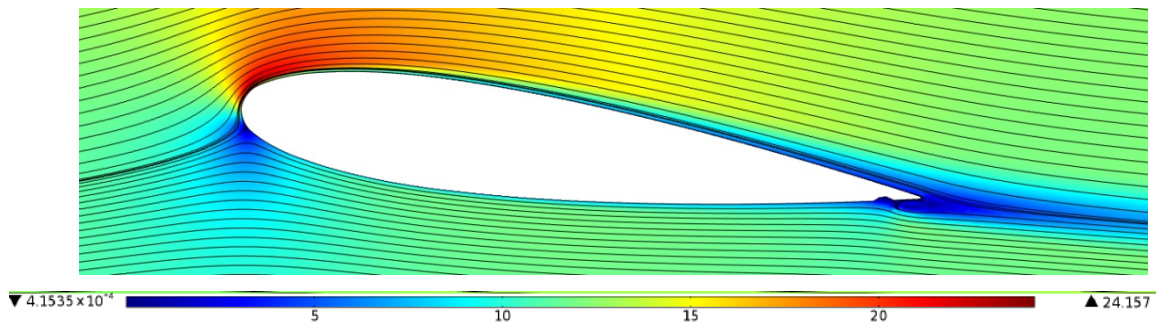


Figure 2.14. Streamlines (superimposed with velocity contour) for NACA 0015 having dimples and flaps at 7° angle of attack.

Chapter 3.

Optimization study

Chapter 2 describes the aerofoil modification effects on the performance of the wind turbine blade. In order to maximize the average torque of the wind turbine blade it is necessary to find an optimized configuration of flap height and dimple radius configuration. The technique of searching for the minimum or maximum value of a given function (which can be called cost/objective function) with varying the dependant parameters or values of that function, incorporating any constraints is called optimization [68]. The goal of the optimization algorithm is to find the true or global minimum or maximum of that objective function efficiently. While solving such types of problems, the objective function may be complex, nonlinear and/or non-differentiable function having too many parameters and design constraints. Typical optimization problems may have infinite number of solutions. Optimization is actually concerned with selecting the best and feasible sets of solution among the entire sets.

3.1. Optimization method

Most real-life optimization problems may have several sets of solutions. Several general approaches to optimization are available as follows: Analytical methods, Graphical methods, Experimental methods, Numerical methods etc. [68]. Analytical method is based on the classical technique of differential calculus. This method cannot be applied to highly nonlinear problems. The graphical method may be used to find the optimized value of the function if the number of variables and constraints do not exceed a few. The optimum value of a function can be achieved by direct experimentation. In this method, the function is set up and adjusted one by one and the performance criterion is measured in each case. This method may lead to optimum or near optimum operating conditions. Moreover, the reliability of this method should be checked. In the

numerical based approach, various search algorithms are employed to generate a series of solutions iteratively starting with an initial estimate for the solution. The process will continue until the convergence criterion is satisfied. Numerical methods can be used to solve highly nonlinear optimization problems which cannot be solved analytically.

3.2. CFD and optimization

In computational fluid dynamics (CFD), numerical methods are applied to solve the fluid flow equations (i.e. Navier-Stokes equations) with appropriate boundary conditions. The problem may be assumed as steady state or transient condition. In this study, the optimization procedure is carried out with the combination of design of experimentation (DOE) and numerical search approach. The DOE values have been obtained from the CFD analysis. As direct aerodynamic optimizations suffer from high computational costs, DOE based optimization can be a good alternative if the response surface has been constructed properly. Objective function evaluation in many engineering problems is costly which makes the optimization task expensive. A popular approach for aerodynamic optimization is to construct, from a selected number of design points, a surrogate of the objective function, to be applied for subsequent optimization. Kim et al. [69] performed such type of optimization technique applied to a two-dimensional channel having periodic ribs.

3.3. Optimization procedure for this study

Having established the enhancement of aerofoil due to the presence of dimple and Gurney flap, this section introduces an optimization procedure in order to maximize the average tangential torque. The optimization procedure is based on Response Surface Approximation (RSA) technique as this takes less computational time. The reliability and applicability of RSM based optimization techniques applied at different fluid flow optimization problems were discussed in many previously published articles [19], [20], [34], [44], [46], [48]–[51], [69].

In this study, the tangential force is used as the objective function at a fixed tip speed ratio, $\lambda=3.5$ for $Re_c= 2.35 \times 10^5$. Previous research work also suggests that the maximum performance of the VAWT blade can be achieved at a tip speed ratio of 3.5 [64]. Further studies can be performed in the future to optimize the performance at different tip speed ratios. To create a response surface, the optimization code takes 16 selected design points (Table 3.1) using the central composite design (CCD) proposed in Myers et al. [45], [70]. The flow chart shows these various steps involved in the optimization process. After constructing the response surface model, a global optimization method, Genetic algorithm (GA) [20], [49], [68], [71], [72] is used to find the optimum value of the problem. A second order polynomial is used to obtain a full quadratic model.

The coefficient of determinant (R^2) for the RSA model is 0.93 which indicates the reliability of the approximation model. The values obtained from the response surface model have also been checked with the CFD simulation results and the values are varied approximately within $\pm 10\%$. Thus, the response surface model is deemed highly reliable and can be used for further analysis of the optimization problem. As the design variable is small (less than four), the RSA algorithm has been developed in such a way that it can take any of the following types of response surface design for the quadratic model [45]: Central composite design (CCD) and Box-Behnken design (BBD). CCD design can also be classified as three types: circumscribed (CCC), inscribed (CCI) and faced (CCF) [70]. After obtaining the response at different data sets, the objective or cost function is then created. As in literature [19], [20], [34], [44]–[51] the response surface is approximated using a quadratic approximation and written as

$$y = a_0 + \sum_{i=1}^n a_i x_i + \sum_{i=1}^n a_{ii} x_i^2 + \sum_{i < j}^n a_{ij} x_i x_j + \varepsilon \quad (3.1)$$

Where,

x_i, x_j are the independent design variables

y is the response surface function

a_0 is the constant parameter

a_i is the parameter that gives the linear effect of x_i

a_{ii} is the parameter that gives the quadratic effect of x_i

a_{ij} is the parameter that gives the interaction between x_i and x_j

ϵ is the fitting error.

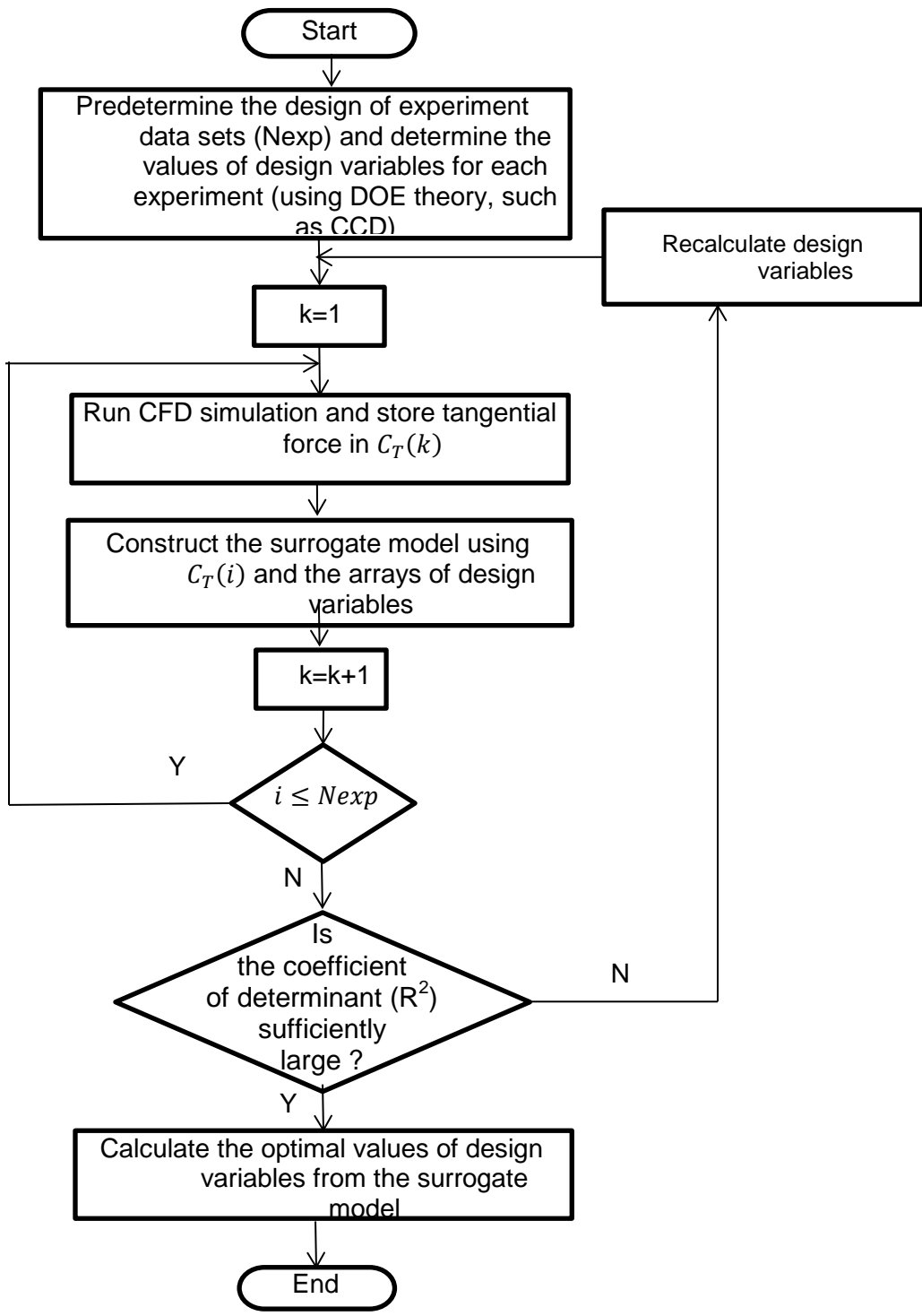


Figure 3.1 . Flow chart of the optimization process.

3.4. Optimization results

In this section, the result of the optimization procedure has been presented. For the RSA, we have chosen the radius of the dimple to be the 1st design variable (x_1), the flap height to be the second design variable (x_2) and the non-dimensional tangential force to be the response (y). The resulting polynomial function is used as the objective function of the optimization problem using Genetic Algorithm (GA). For the GA, a population size of 50, a crossover fraction of 0.8, mutation rate of 0.1, and number of generations of 1500 are assumed. Table 3.1 shows the tangential force coefficient values for different data sets using the CCD design analysis. In the present case, the CCF design is good enough to create a reliable response surface. After obtaining the response at different data sets, the objective function is then created and the results are shown in Table 3.3. From Table 3.4 it can be seen that aerofoil having dimple radius 0.006 m and flap height having 0.008 m gives the best performance.

Table 3.1 Response results of selected experimental data sets

Trial No	Designed Parameters		Response Parameter, y (Non-dimensional Tangential Force)
	X_1 (m)	X_2 (m)	
1.	0.001	0.002	0.031
2.	0.001	0.008	0.037
3.	0.006	0.002	0.039
4.	0.006	0.008	0.048
5.	0.006	0.005	0.035
6.	0.006	0.005	0.034
7.	0.0035	0.002	0.0345
8.	0.0035	0.008	0.0375
9.	0.0035	0.005	0.033

Table 3.2 shows the results of the ANOVA (Analysis of variance) analysis performed in MATLAB [73]. ANOVA examines the sensitivity of the cost function to each input variable by analyzing the p-value (indicates the level of significance) of the response surface. Normally in statistics, the response surface approximation results are considered to be significant if the p-value is less than 0.05 [74]. Smaller p-value indicates higher sensitivity to the response surface. For the present study, p-value for the dimple radius is 0.0461 and flap height is 0.0252 which indicate that both design variables have significant effects on the performance of the wind turbine.

Table 3.2 ANOVA results

Design Variable	p-value
Dimple radius, (x_1)	0.0461
Flap Height (x_2)	0.0252

Table 3.3 RSA Result

a_0	0.026
a_1	1.555
a_2	0.703
a_{11}	-0.4198
a_{22}	-0.239
a_{12}	-0.0596

Table 3.4 Optimized Value

Design Variable	Lower Bound	Upper Bound	Optimized Value
Dimple radius, (x_1)	0.001 (m)	0.006 (m)	0.006 (m)
Flap Height (x_2)	0.002 (m)	0.008 (m)	0.008 (m)
Non dimensional Tangential Force (y)			0.041

Figure 3.2 shows the tangential force coefficient at different iterations of the optimization process. It is seen from the figure that 51 generations are needed to reach the optimized (maximized) tangential force. The optimization process has also been checked with another global optimization algorithm termed as “Simulated annealing algorithm” [75] and similar results has been obtained (Figure 3.3). Figure 3.3 also indicates that simulated annealing algorithm (needs 8 iteration) is more efficient than the genetic algorithm (needs 40 iteration) for the present study while predicting maximum function value.

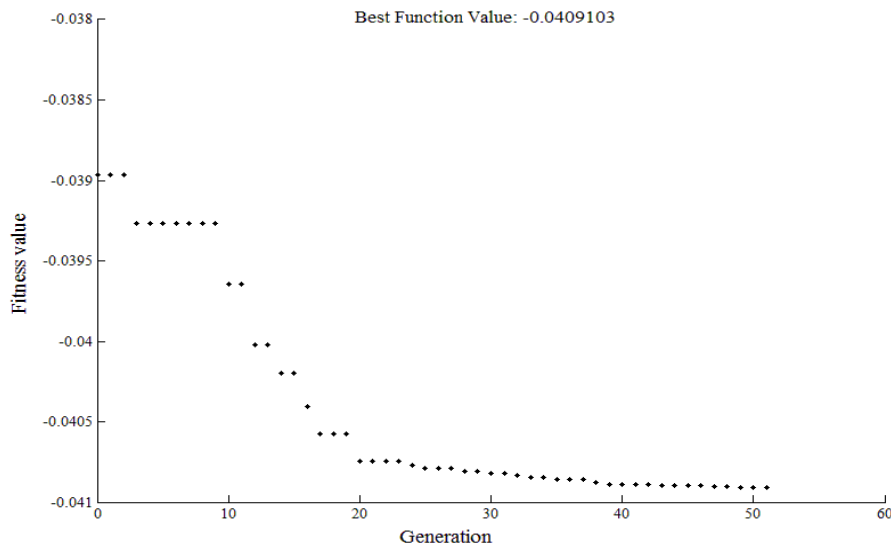


Figure 3.2. Optimization (maximization) history for Genetic algorithm: force coefficient values at different iteration (generation).

Figure 3.4 and Figure 3.5 compare the performance of optimized aerofoil with the base NACA 0015 aerofoil. From the figures it is seen that the modified and optimized shape of the aerofoil generates a larger tangential force than the baseline aerofoil NACA 0015. This is a result of the dimple and Gurney flap being introduced at the lower surface of the aerofoil, which results in a much larger lift force at a positive angle of attack even up to the stall condition (12° angle of attack) as seen from Figure 3.5. Subsequently, the optimized aerofoil shows significantly larger values of lift coefficient for azimuthal angle approximately up to 200° . Due to the lower value of negative angle of attack, beyond the azimuthal angle of 210° , the optimized aerofoil only moderately

outperforms the base NACA 0015 aerofoil. In total, the average tangential force obtained for the optimized aerofoil is almost 35% larger than the base NACA 0015 aerofoil.

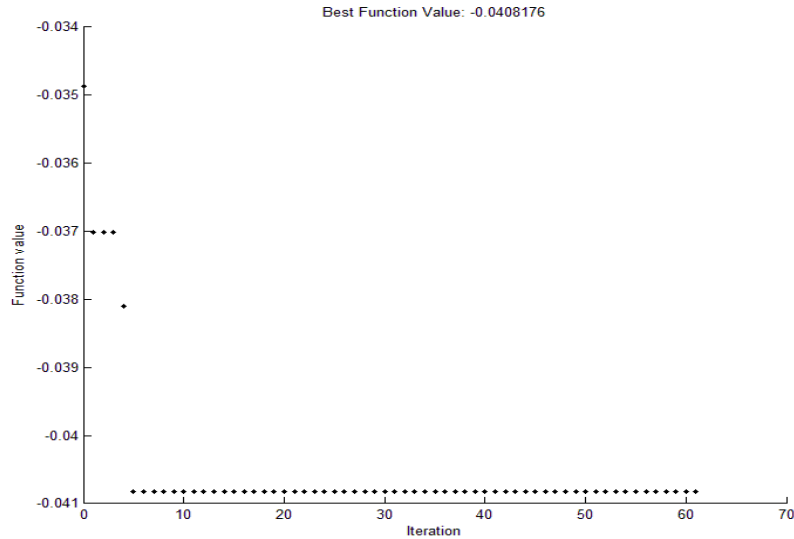


Figure 3.3. Optimization (maximization) history for Simulated Annealing algorithm: force coefficient values at different iterations.

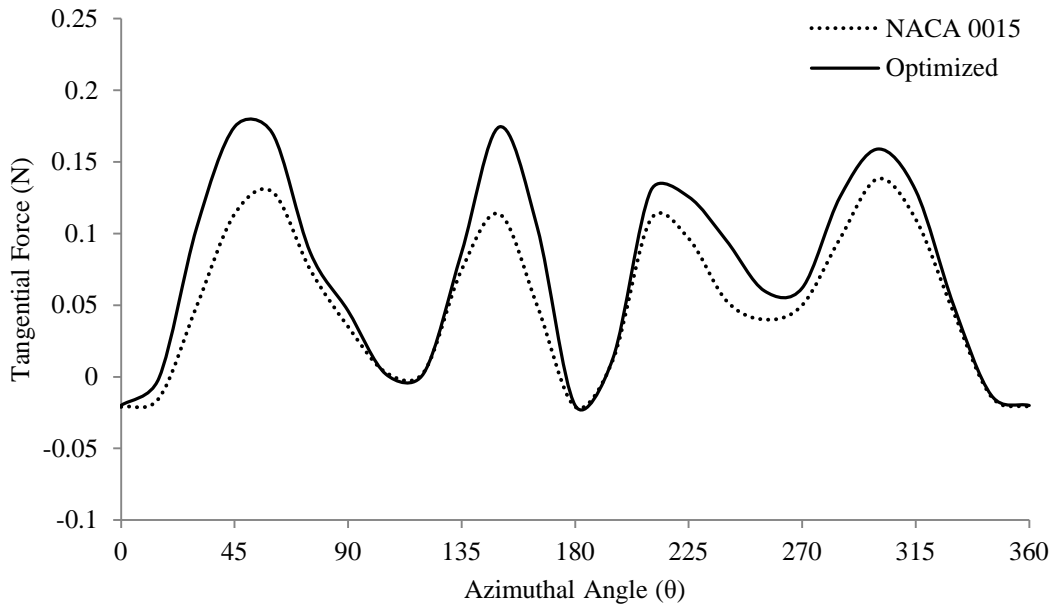


Figure 3.4. Tangential Force Variation at different azimuthal angle.

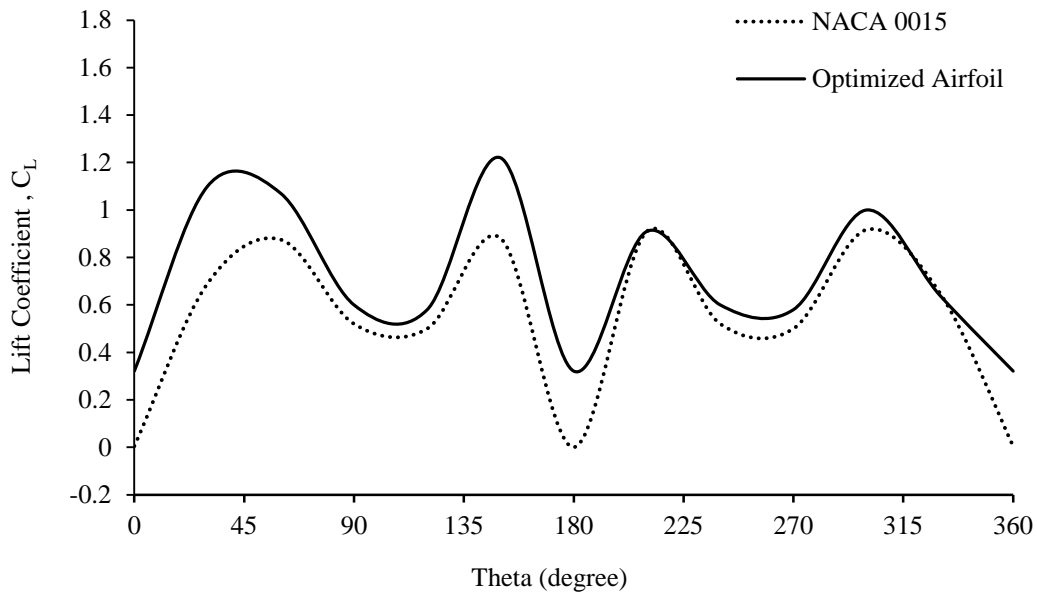
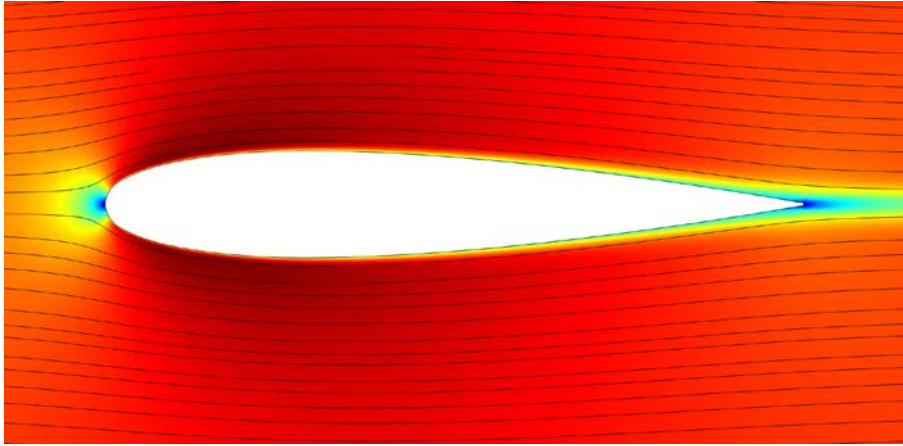


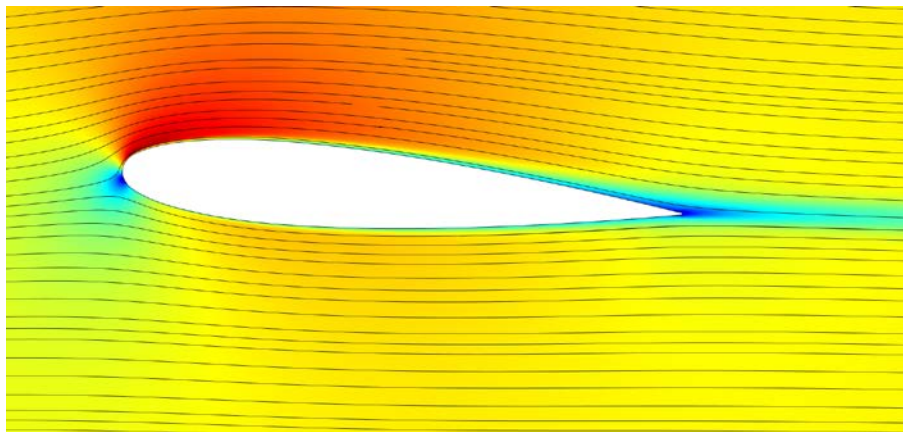
Figure 3.5. Variation of lift coefficient at different azimuthal angle.

Dimples and Gurney flaps are employed to create greater turbulence that results in creating the flow recirculation near the aerofoil trailing edge. Figure 3.6 and Figure 3.7 show the velocity contours as well as flow streamlines at different azimuthal angles for the baseline NACA 0015 and the optimized aerofoil respectively. At a larger angle of attack boundary layer separation and flow recirculation are observed. It is seen by comparing Figure 3.6 (e) and Figure 3.7 (e) that the optimized aerofoil has generated higher pressure at lower surface and larger suction at the upper surface of the aerofoil. Figure 3.8 indicates that at $\theta=60^\circ$, a significant amount of flow separation has been observed for the standard NACA 0015 aerofoil but the optimized aerofoil still exhibits attached flow. Additionally, the optimized aerofoil exhibits larger turbulence generation than the base NACA 0015 aerofoil due to the combined effects of dimple and Gurney flap. Figure 3.8 shows the flow recirculation generated for the dimple and flap configuration near the trailing edge of the optimized aerofoil. This flow recirculation increases the lift force specifically at a positive angle of attack and thus increases the tangential force value. From Figure 3.6 and Figure 3.7 it is also seen that for the optimized aerofoil, the upper surface suction and lower surface pressure are much higher than the base NACA 0015 aerofoil which thereby increases the lift coefficient values. Having demonstrated the improved performance of the optimized aerofoil for

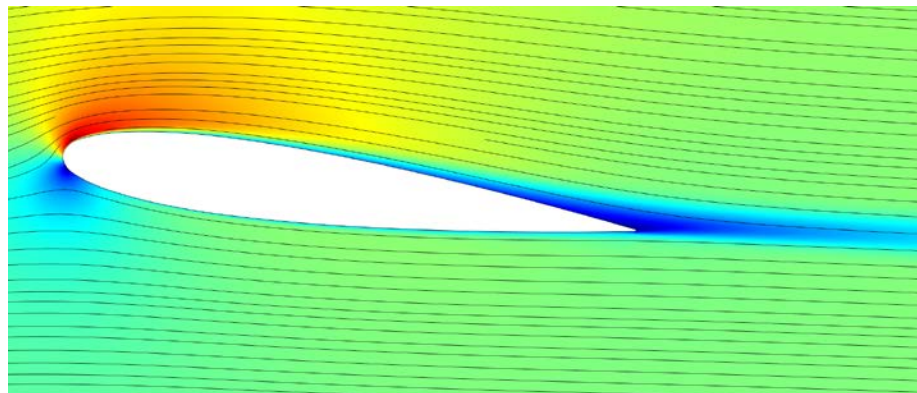
steady-state conditions, results under dynamic conditions will also be tested and presented in the next sections.



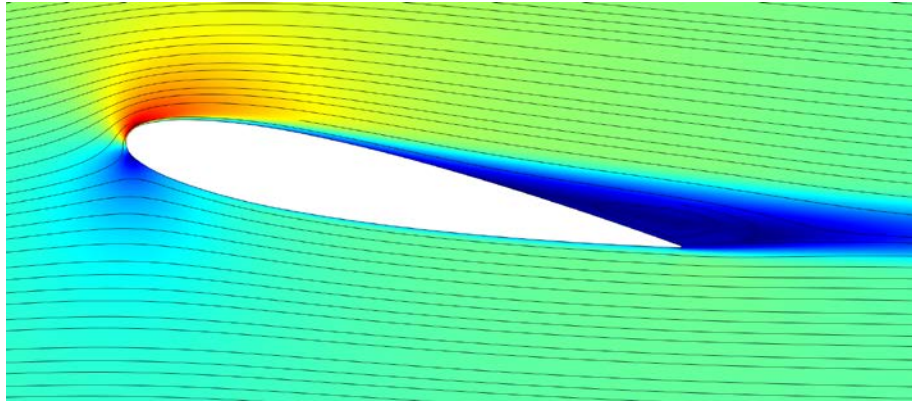
(a) $\theta = 0^\circ$



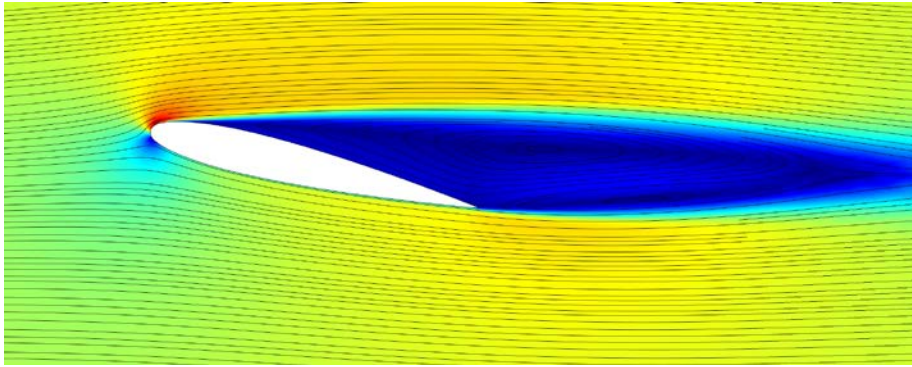
(b) $\theta = 15^\circ$



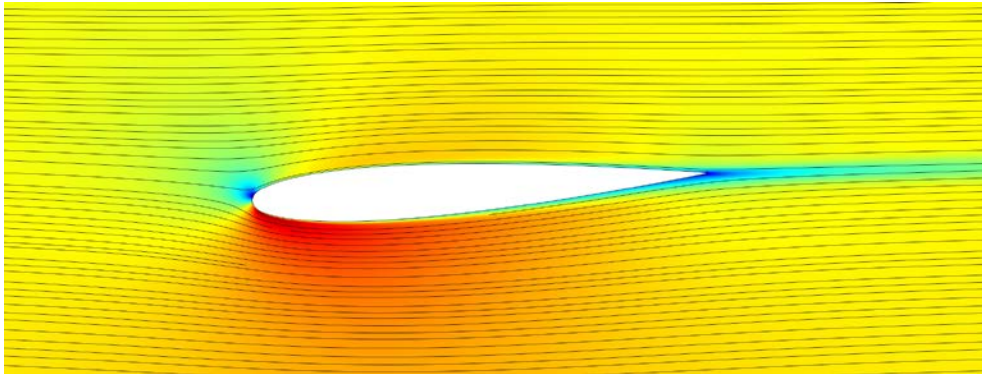
(c) $\theta = 45^\circ$



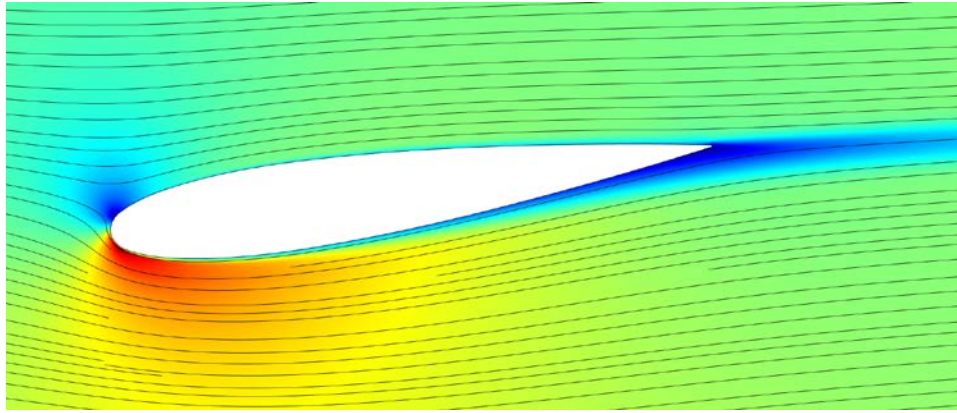
(d) $\theta = 60^\circ$



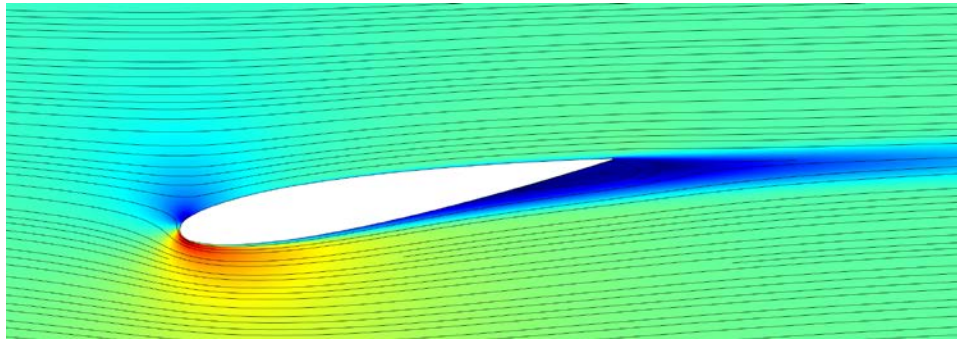
(e) $\theta = 105^\circ$



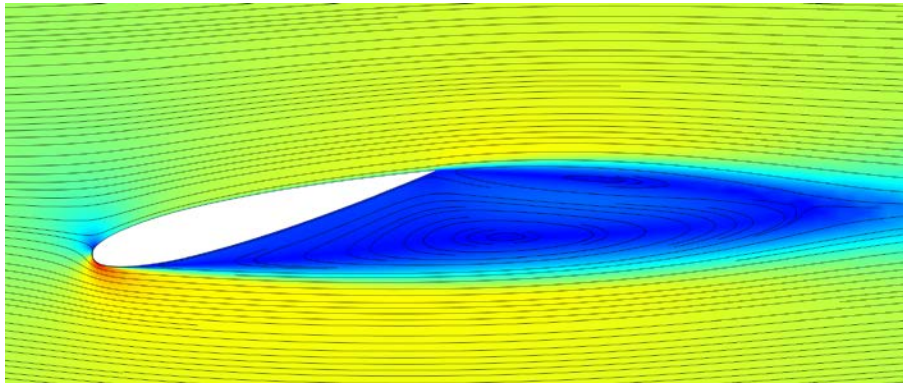
(f) $\theta = 195^\circ$



(g) $\theta = 210^\circ$



(h) $\theta = 225^\circ$



(i) $\theta = 255^\circ$

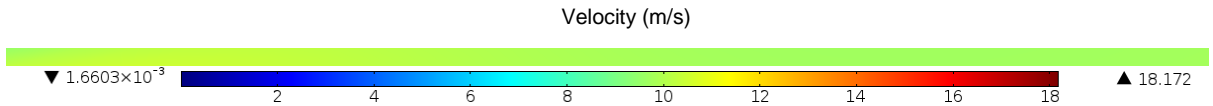
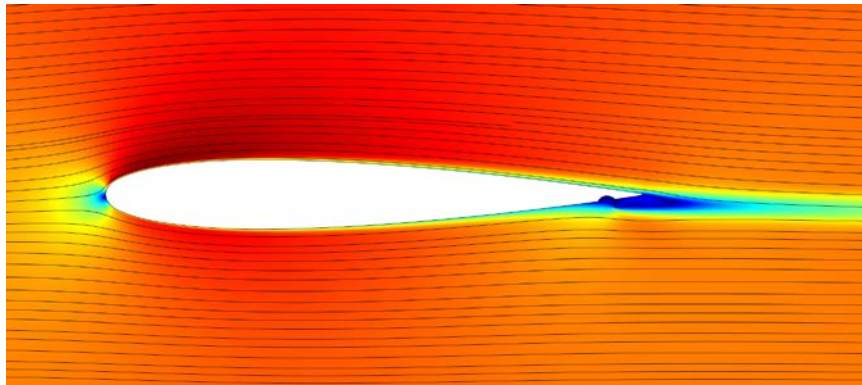
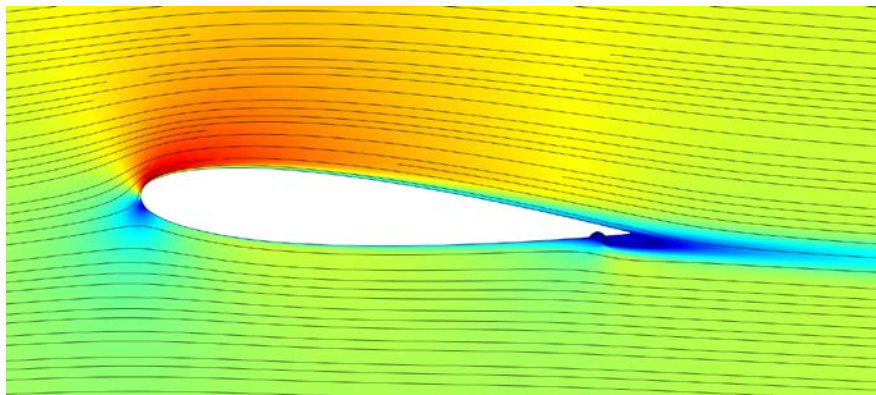


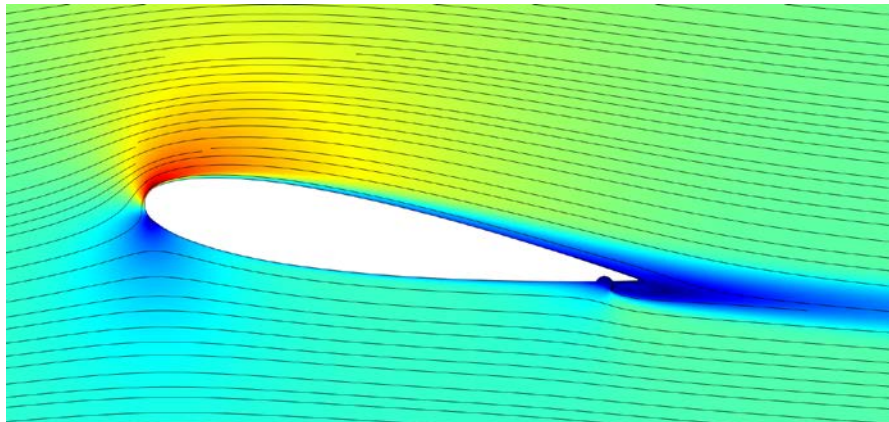
Figure 3.6. Velocity contour superimposed with flow streamlines for NACA 0015 at various azimuthal angles.



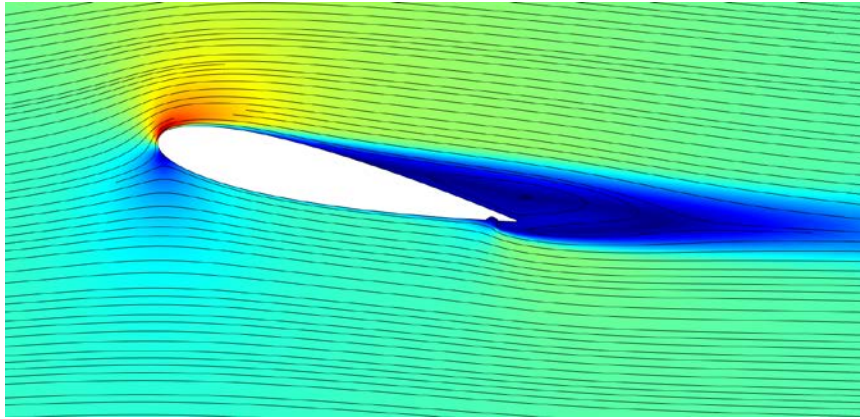
(a) $\theta = 0^\circ$



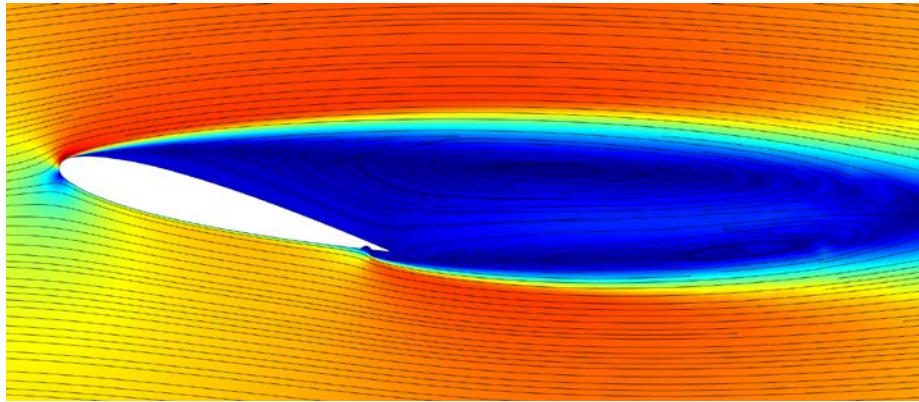
(b) $\theta = 15^\circ$



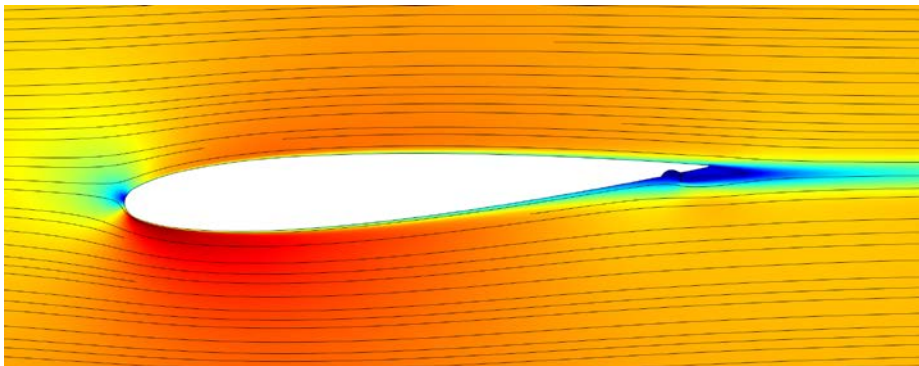
(c) $\theta = 45^\circ$



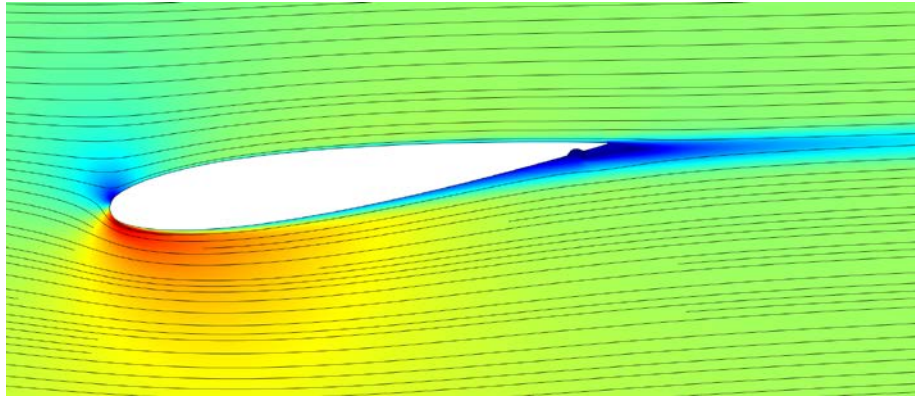
(d) $\theta = 60^\circ$



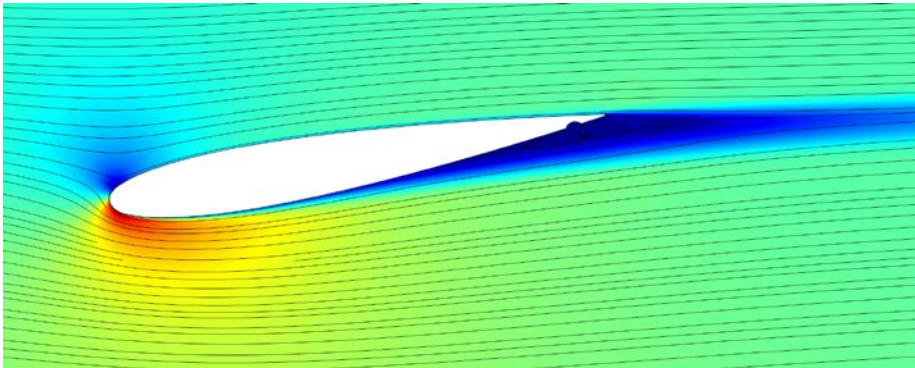
(e) $\theta = 105^\circ$



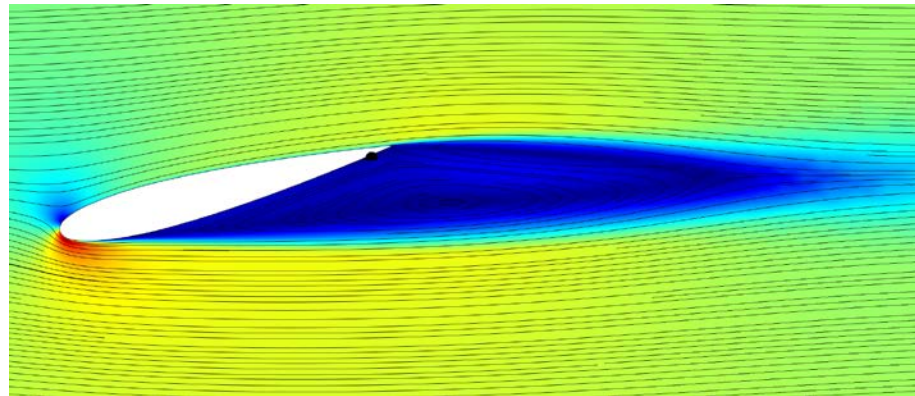
(f) $\theta = 195^\circ$



(g) $\theta = 210^\circ$



(h) $\theta = 225^\circ$



(i) $\theta = 255^\circ$

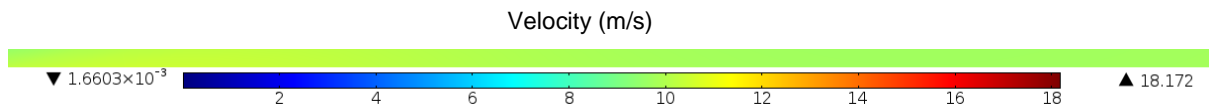
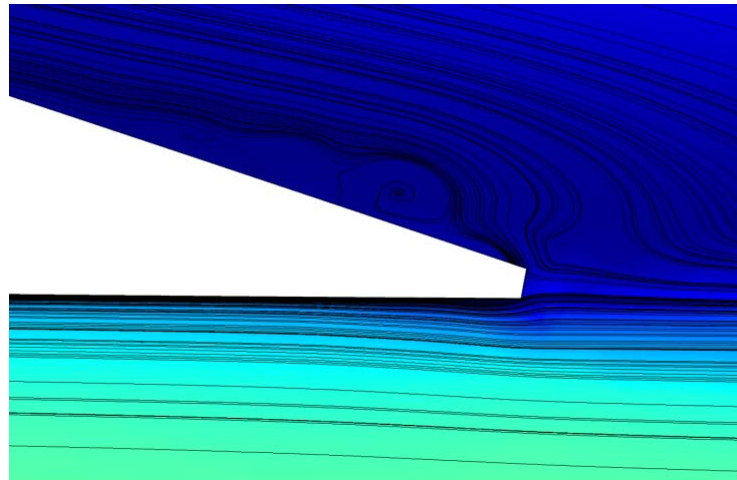
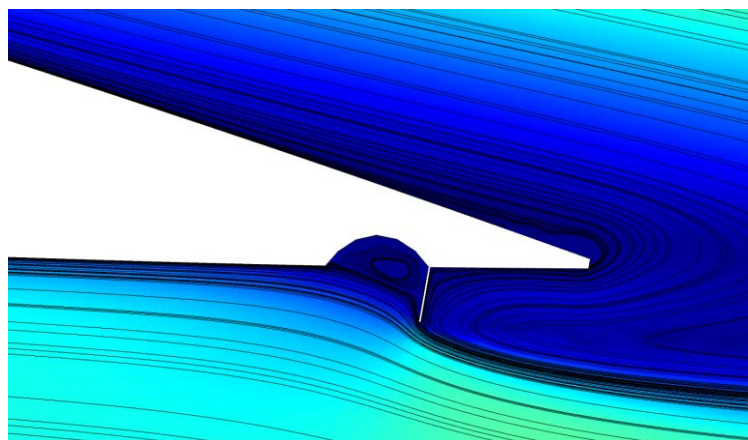


Figure 3.7. Velocity contour superimposed with flow streamlines for the optimized aerofoil at various azimuthal angles.



(a)



(b)

Figure 3.8. Flow separation (superimposed with velocity contour) near the trailing edge for the (a) standard NACA 0015 and (b) optimized aerofoil at azimuthal angle, $\theta = 60^\circ$.

Chapter 4.

Parametric study: Dynamic condition analysis

The cyclic variation of the local angle of attack for the case of vertical axis wind turbine is very similar to the flow field around a pitching aerofoil. Figure 4.1 shows the cyclic variation of the local angle of attack at different orbital (azimuthal) angle of the VAWT motion. It is also seen at that lower tip speed ratios, the local angle of attack is greater than the higher tip speed ratios.

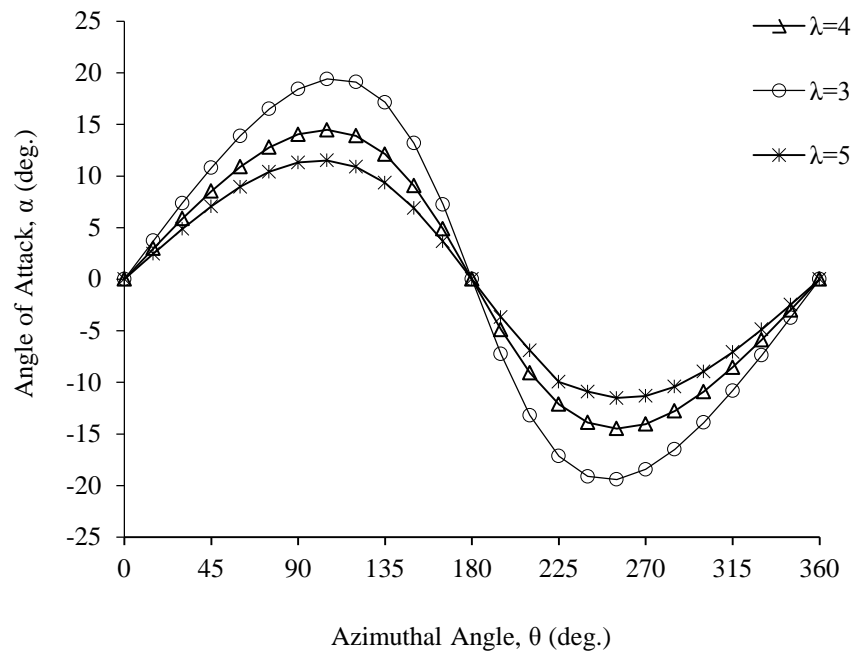


Figure 4.1. Angle of attack as a function of azimuthal angle at different tip speed ratios.

A large number of experimental studies have been carried out to predict the flow field around the pitching aerofoil at different Reynolds number for various applications

[15], [16], [22], [23], [76], [77]. At low tip speed ratio case for VAWTs (i.e. larger angle of attacks), greater vortex and flow separation incidence have been observed on the surfaces of the aerofoil. The vortex created at larger AOA, moves along the aerofoil surface during the dynamic pitching cycle. This causes the increase of the boundary layer thickness and in turn massive flow separation phenomenon is observed. The larger the AOA, the greater the vortex has been generated. Due to the massive flow separation the aerofoil cannot generate lift after a certain point and eventually the tangential force becomes to decrease. This phenomenon can be referred as “dynamic stall” condition [23]. In addition to the dynamic stall effect, VAWTs also experiences the fluid–structure interaction occurrence, since VAWT blade has the cyclic motion along the generated wake developed at the upstream period of the cycle. Thus, to predict such type of flow behaviour is challenging. Proper modeling of the turbulent flow and fine grids are required to capture the fluid-structure interaction accurately. In this study, the aerofoil modification effects is analyzed for only light stall conditions (AOA< 20⁰) i.e. at moderately high tip speed ratio to avoid the massive flow separation at deep dynamic stall which occurs at very high angle of attacks (>20⁰) [23].

4.1. Problem statement

As the blade rotates in a VAWT, the direction and magnitude of the effective wind velocity change in a cyclic manner. Figure 4.2 shows a simple schematic of the single aerofoil pitching motion which is similar to the VAWT blade. Thus, the oscillatory motion (pitching oscillation) of the blade can be assumed as-

$$\alpha = \alpha_{\text{mean}} + \alpha_{\text{amp}} \sin(\omega t) \quad (4.1)$$

Where,

α_{mean} = mean angle of attack

α_{amp} = pitch oscillation amplitude

ω = angular velocity.

$k = \text{reduced frequency, } \frac{\omega c}{2U_\infty}$

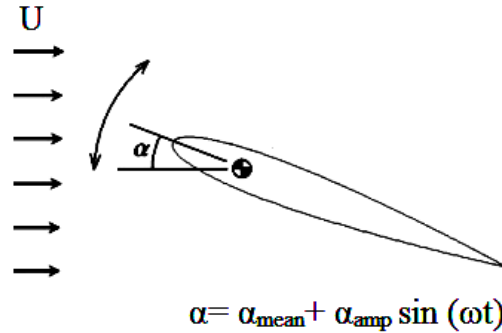
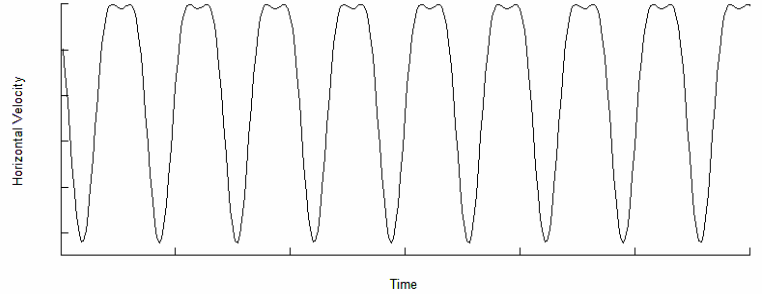


Figure 4.2. Simple schematic of the aerofoil pitching motion.

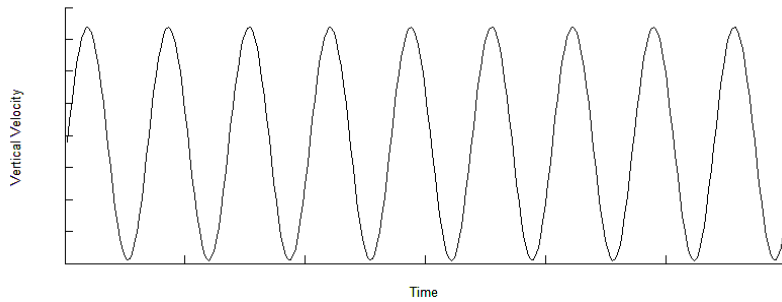
4.2. Numerical techniques and method of analysis

Previous literature has used different values of frequencies and oscillating amplitudes to analyze the wind turbine performance [15], [16], [22], [23], [18], [59]. For the present unsteady CFD simulation, the aerofoil is kept aligned with the horizontal axis. The horizontal and vertical components of the boundary conditions are modified to alter the direction of the far-field flow over the aerofoil at every time step. The mean angle of attack is set to 8° and amplitude is set to 10.6° . The horizontal and vertical velocity components of the sinusoidal pitching motions are shown in Figure 4.3. In this thesis the performance of the aerofoils has been analyzed for light dynamic stall conditions only (up to 18.6° angle of attack). The performance of the optimized aerofoil has been analyzed at two different chordal Reynolds number, $Re_c = 2.35 \times 10^5$ and 3.6×10^5 . Very few experimental studies have been found to analyze the aerofoil performance light dynamic stall conditions at these low Reynolds numbers ($Re_c \leq 10^6$). From the experimental study of Lee et al. [23], it can be said that deep dynamic stall occurs at a higher angle of attack ($>20^\circ$) in comparison with the static stall condition ($>12^\circ$). Under light dynamic conditions, almost attached flow or moderate flow separations have been observed even at the 18° angle of attack. For this reason, the revised k- ω turbulence model [58] has been used to capture the flow condition for the current oscillating dynamic condition as this model is capable to capture the flow

parameters accurately at moderate pressure gradients with moderate flow separation [11], [24]. The angular frequency of the oscillation has been assumed to be 18.67 rad/s.



(a)



(b)

Figure 4.3. Sinusoidal free stream (inlet) velocity (a) Horizontal and (b) Vertical velocity field.

The revised k - ω model [24] solves for the turbulent kinetic energy, k , and for the dissipation per unit turbulent kinetic energy, ω . In the CFD simulation software COMSOL [24], the revised k - ω model uses the wall function near the aerofoil wall while the SST k - ω model does not use the wall function. For this reason revised k - ω model is computationally more efficient than the SST k - ω model specifically for light dynamic stall conditions. The revised k - ω model solves for the turbulent kinetic energy, k , and for the dissipation per unit turbulent kinetic energy, ω . The Wilcox revised k - ω model [24], [58] are described as follows:

$$\rho \frac{\partial k}{\partial t} + \rho u \cdot \nabla k = P_k - \rho \beta^* k \omega + \nabla \cdot ((\mu + \sigma^* \mu_T) \nabla k) \quad (4.2)$$

$$\rho \frac{\partial \omega}{\partial t} + \rho u \cdot \nabla \omega = \alpha \frac{\omega}{k} P_k - \rho \beta \omega^2 + \nabla \cdot ((\mu + \sigma \mu_T) \nabla \omega) \quad (4.3)$$

Here,

$$\mu_T = \rho \frac{k}{\omega}$$

$$\alpha = \frac{13}{25}, \beta = \beta_0^* f_\beta, \quad \sigma = \frac{1}{2}, \sigma^* = \frac{1}{2}$$

$$\beta_0 = \frac{13}{125}, \quad f_\beta = \frac{1 + 70\chi_w}{1 + 80\chi_w}$$

$$\chi_w = \left| \frac{\Omega_{ij} \Omega_{jk} S_{ki}}{(\beta_0^* \omega)^3} \right|$$

$$\beta_0^* = \frac{9}{100}, \quad f_{\beta_0^*} = \begin{pmatrix} 1 & ; \chi_k \leq 0 \\ \frac{1 + 680 \chi_k^2}{1 + 400 \chi_k^2} & ; \chi_k > 0 \end{pmatrix}; \chi_k = \frac{1}{\omega^3} (\nabla k \cdot \nabla \omega)$$

Ω_{ij} is is the mean rotation-rate tensor:

$$\Omega_{ij} = \frac{1}{2} \left(\frac{\partial \bar{u}_i}{\partial x_j} - \frac{\partial \bar{u}_j}{\partial x_i} \right)$$

and S_{ij} is the mean strain-rate tensor:

$$S_{ij} = \frac{1}{2} \left(\frac{\partial \bar{u}_i}{\partial x_j} + \frac{\partial \bar{u}_j}{\partial x_i} \right)$$

The wall function used for this turbulent flow simulation is such that the computational domain is assumed to start a distance y from the wall. The distance y is computed iteratively by solving the following [24]-

$$y^+ = \frac{\rho u_\tau y}{\mu}$$

Where, the friction velocity (u_τ) is assumed such that:

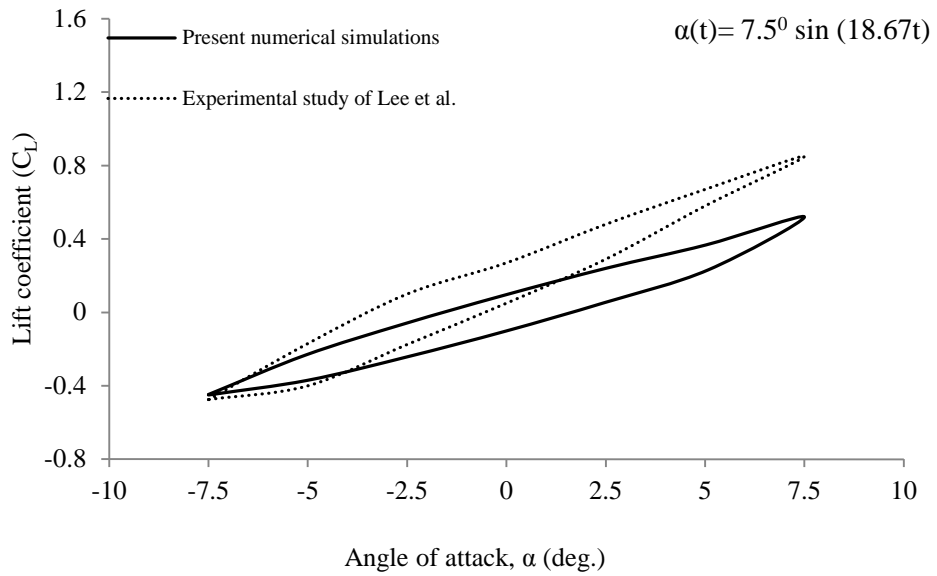
$$\frac{|u|}{u_\tau} = \frac{1}{\kappa} \log y^+ + B \quad (4.4)$$

Here, κ is the von Karman constant whose value is 0.41 and B is an empirical constant equals to 5.2. For the computation the friction velocity u_τ is assumed to be equivalent to $\beta_0^{*1/4} \sqrt{k}$ which becomes 11.06 and the boundary condition for ω can be defined as $\rho.k/(\kappa y^+ \mu)$. This corresponds to the distance from the wall where the logarithmic layer meets the viscous sub-layer. The solutions are always checked in such that the y^+ value is 11.06 on all the walls of the aerofoil [24]. As SST $k-\omega$ model does not use wall function, the y^+ value on near wall region should be ≤ 1 [22], [24]. For this reason more fine mesh is necessary at the near wall region while using the SST $k-\omega$ model. Thus, SST $k-\omega$ model takes more time to converge than the revised $k-\omega$ turbulence model but SST $k-\omega$ model gives high accuracy especially at adverse pressure gradients and highly separating flow [11], [24] which is seen at deep dynamic stall conditions having larger AOA ($> 20^\circ$) [23].

4.3. Validation studies for the dynamic case

From previous literature review study it is seen that lift coefficient values are very sensitive to the oscillating frequency values as well as the turbulence intensities [16], [22], [18], [59]. For this reason, turbulence modeling under dynamic and pitching oscillation condition is still an active area of research. Still no such turbulence model is available to predict accurately the flow behaviour of an aerofoil under dynamic oscillation condition [15], [16], [18], [22], [59]. Considering all of the above conditions, the results of the present studies are validated against the experimental study of Lee et al. [23], [59]

and the results are shown in Figure 4.4. This is the only experimental study which has been carried out at low Reynolds number cases (order of 10^5) which is appropriate for the analysis of VAWT. It is seen from Figure 4.4 that the simulations are in reasonable agreement with the experiments. Though at relatively higher angle of attacks the results are not accurate but the overall trend of the results are similar. Various research works is still going on to predict the results under dynamic conditions accurately [15], [16], [18], [22]. These researchers validated the results for low Reynolds number cases, but for the numerical simulations they used very large AOA ($>20^\circ$). To the best knowledge of the author, this work is the first study to validate the CFD results of Lee et al. [23], [59] with the light dynamic stall cases (AOA $< 20^\circ$) at low Reynolds number conditions [76], [78].



(a)

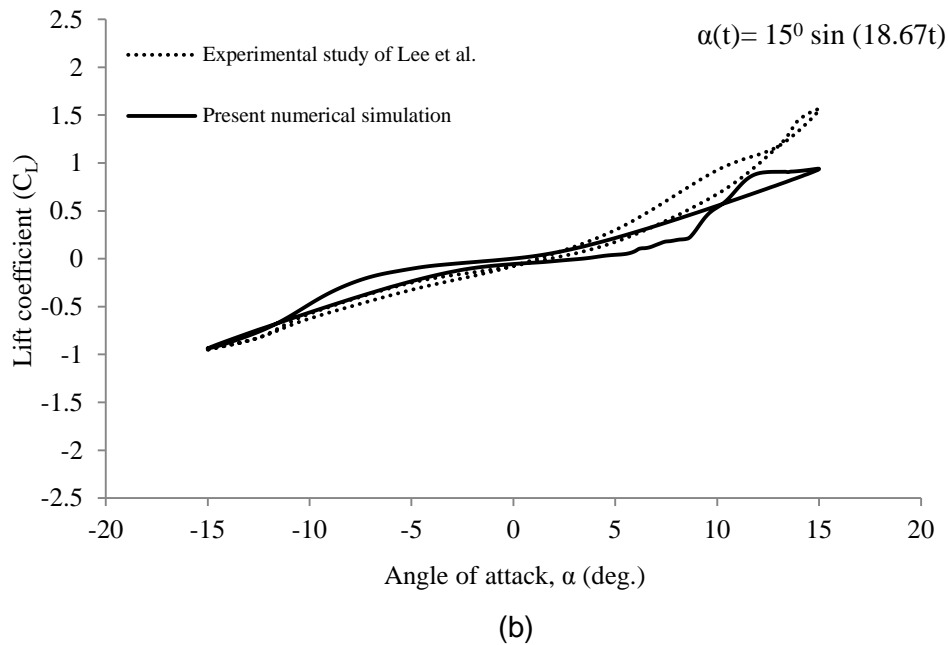


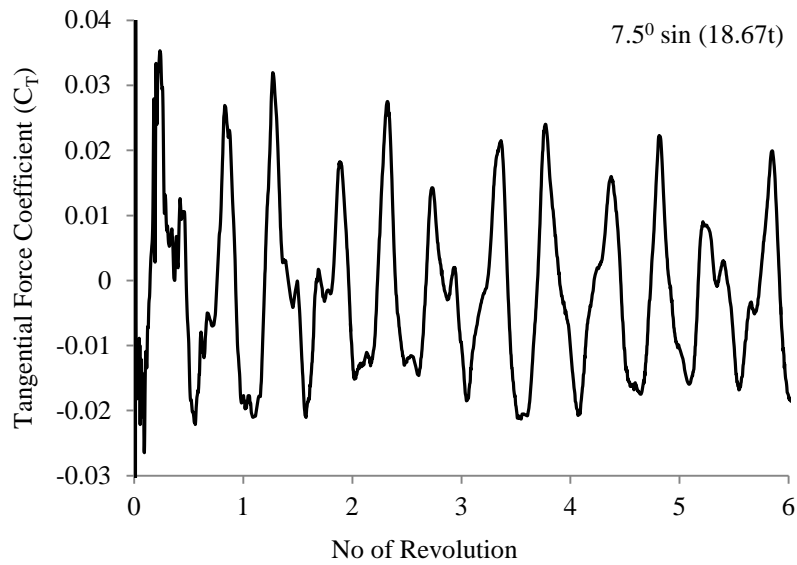
Figure 4.4. Comparison of lift coefficient between previously published experimental study [23], [59] and current numerical simulation at $Re_c = 1.35 \times 10^5$ for oscillating motion: (a) $7.5^\circ \sin(18.67t)$; (b) $15^\circ \sin(18.67t)$.

4.4. Performance of NACA 0015 aerofoil under pitching oscillation

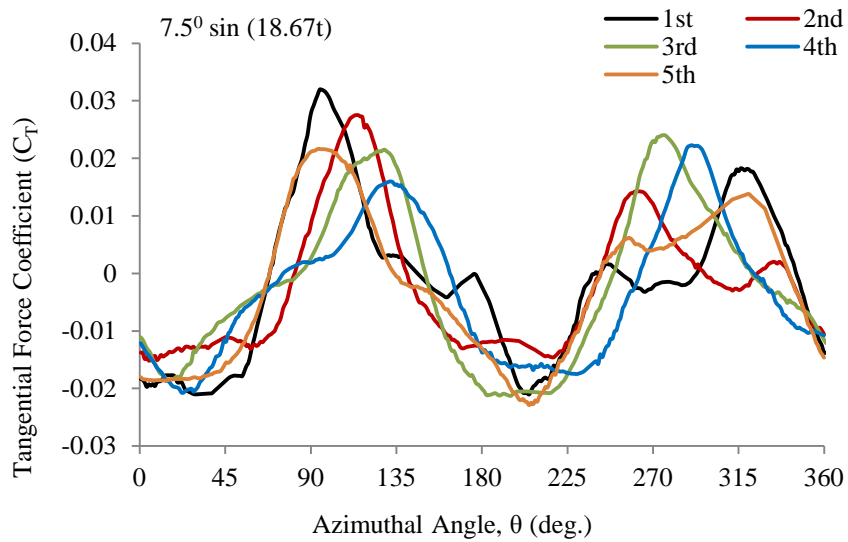
To the best of the author knowledge, no research work has been found to analyze the flow behaviour of the standard NACA 0015 under oscillating pitching condition at low Reynolds number flow. Thus, in this section the simulation has been performed at $k = 0.3734$ and 0.8378 for the aerofoil NACA 0015 at chord Reynolds number 2.35×10^5 . The mean angle of attack is assumed to be zero and two different amplitudes have been assumed to be 7.5° and 16.6° .

Figure 4.5 - Figure 4.8 show the tangential force coefficient at different flow condition for NACA 0015 aerofoil. From these figures it is seen that all the simulation shows almost quasi-steady state behaviour after four revolutions. It can also be said that for higher oscillation frequency, the value of tangential force coefficient is larger. From

Figure 4.8 it is seen that the results are little unsteady even after six or seven cycles of oscillations. This unsteady nature can be described while analyzing the streamlines around the aerofoil surface. Figure 4.9 shows the streamlines around the aerofoil surface for different oscillating condition. From Figure 4.9 (g) it can be seen that flow recirculation begins at the trailing edge for oscillations with the larger angular velocity and amplitude. This flow recirculation may be responsible for the unsteady behaviour of the aerofoil at larger angular speed (41.89 rad/s). It should be noted that none of the cases exhibit stall condition (even at high angle of attack such as 16.6°).

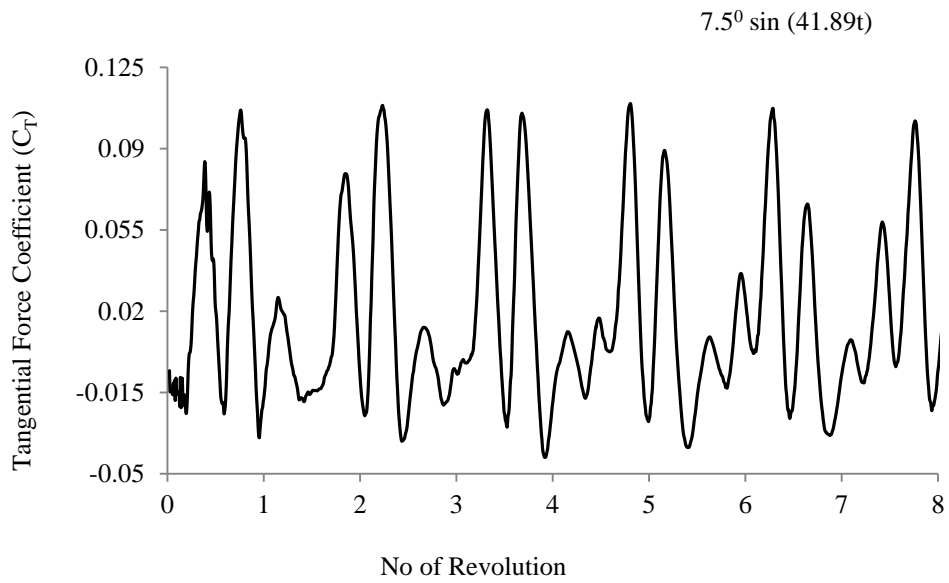


(a)

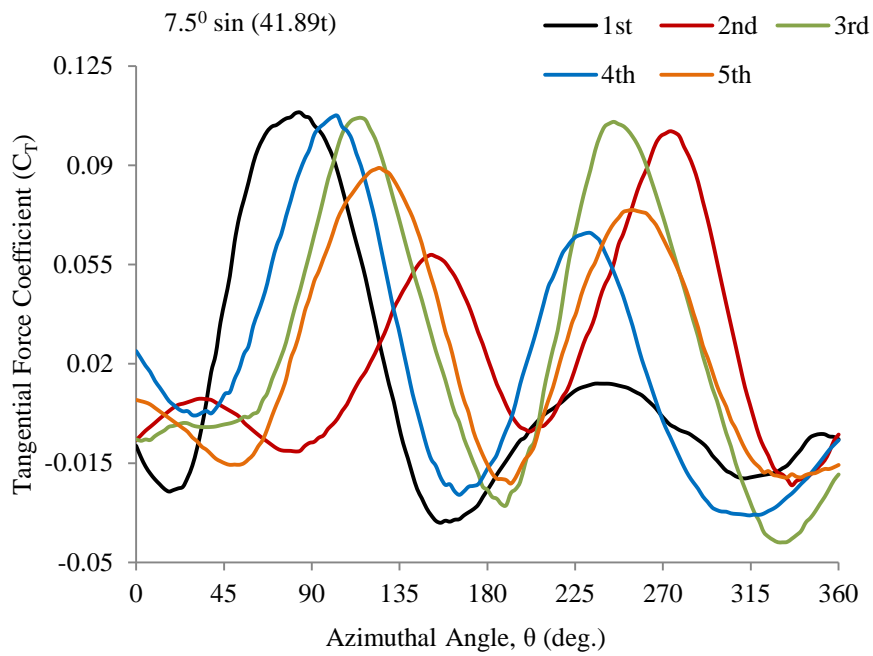


(b)

Figure 4.5. Tangential Force Coefficient at different (a) revolution and (b) azimuthal Angle for the condition $7.5^0 \sin(18.67t)$.

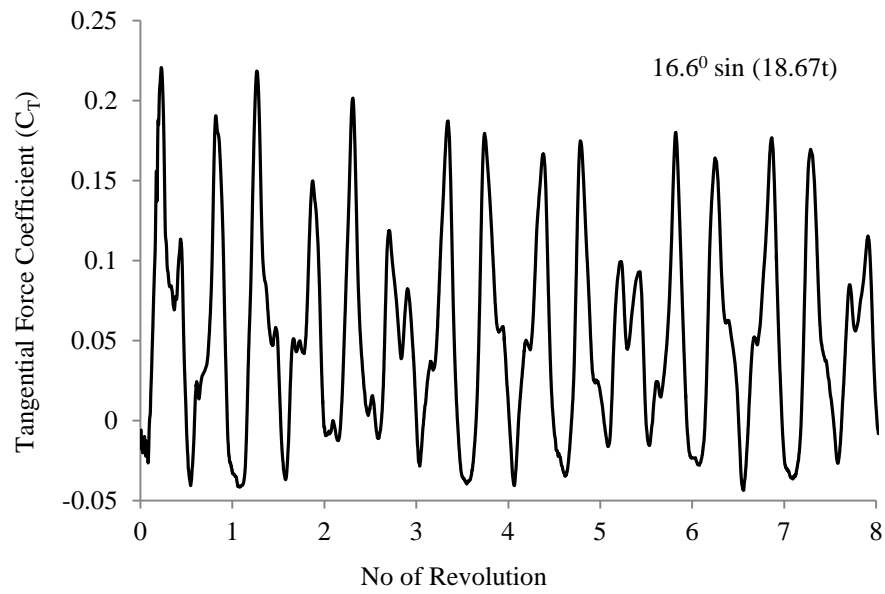


(a)

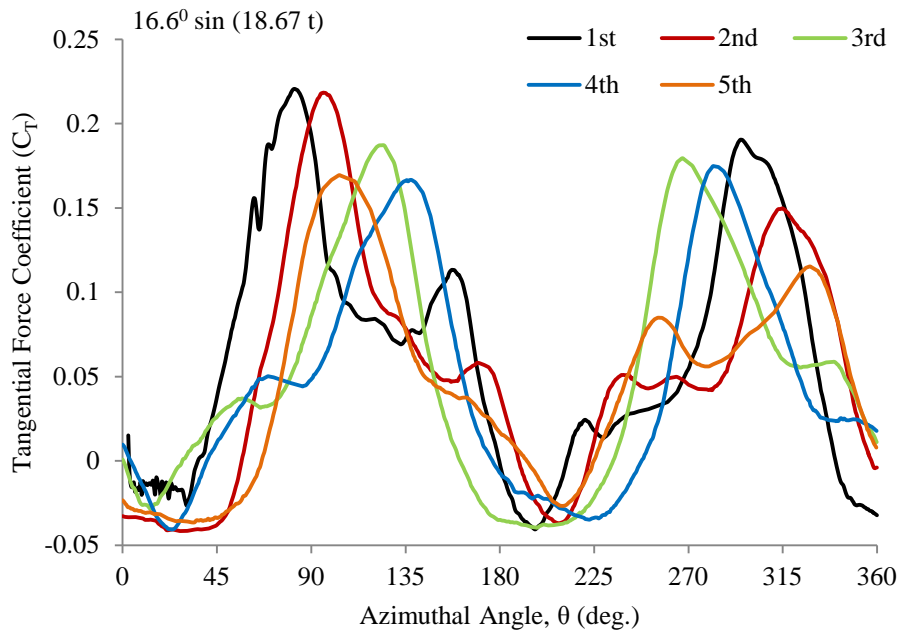


(b)

Figure 4.6. Tangential Force Coefficient at different (a) revolution and (b) Azimuthal Angle for the condition $7.5^0 \sin(41.89t)$.

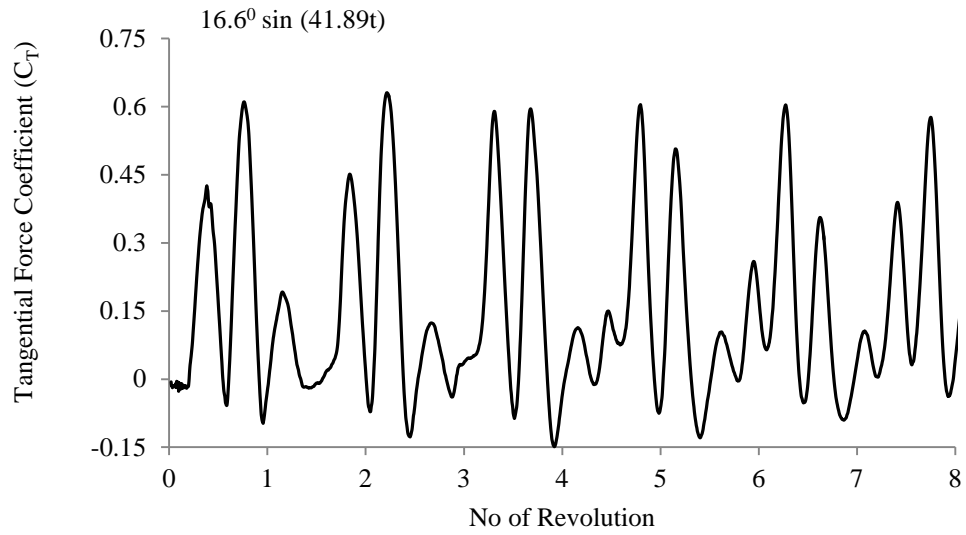


(a)

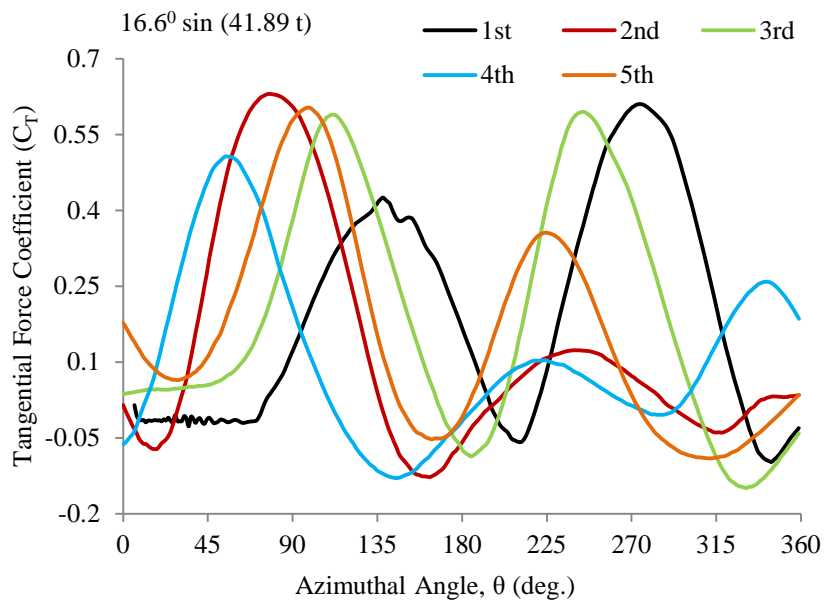


(b)

Figure 4.7. Tangential Force Coefficient at different (a) revolution and (b) azimuthal Angle for the condition $16.6^0 \sin (18.67t)$.

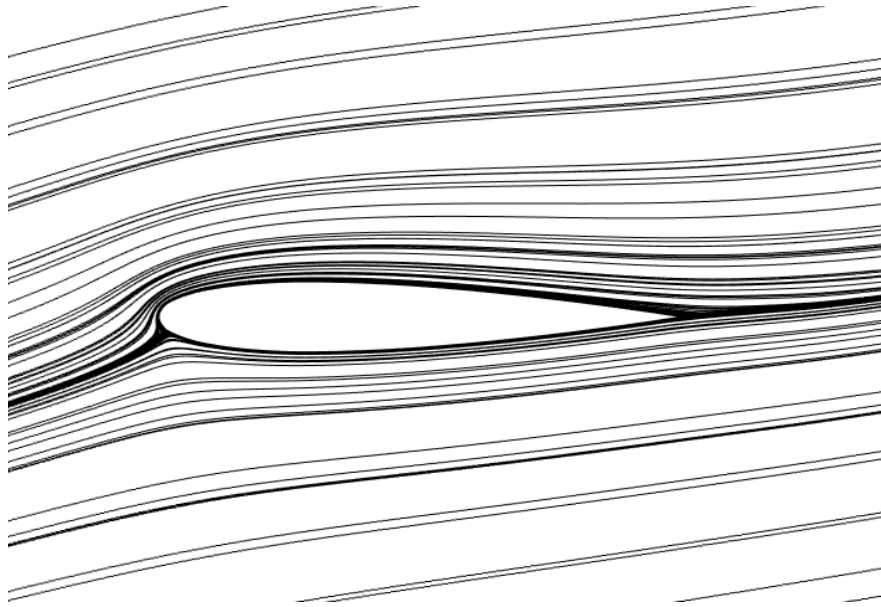


(a)

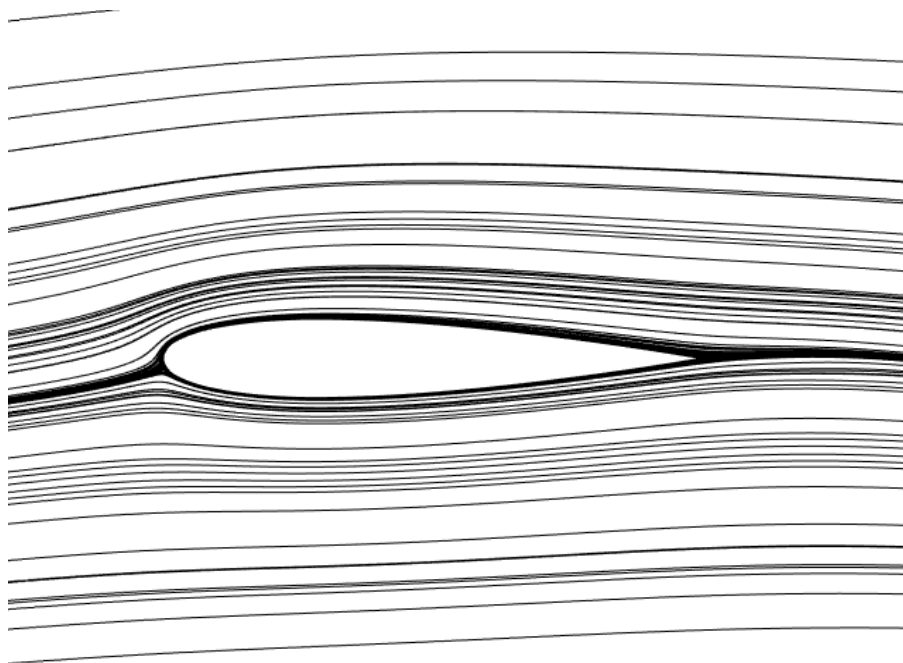


(b)

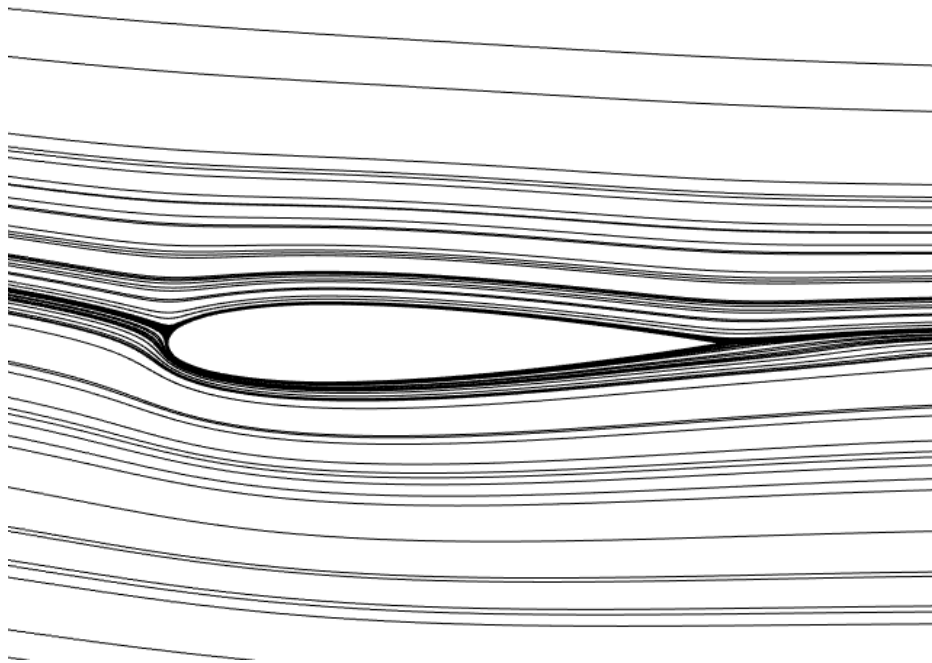
Figure 4.8. Tangential Force Coefficient at different (a) revolution and (b) azimuthal Angle for the condition $16.6^0 \sin(41.89t)$.



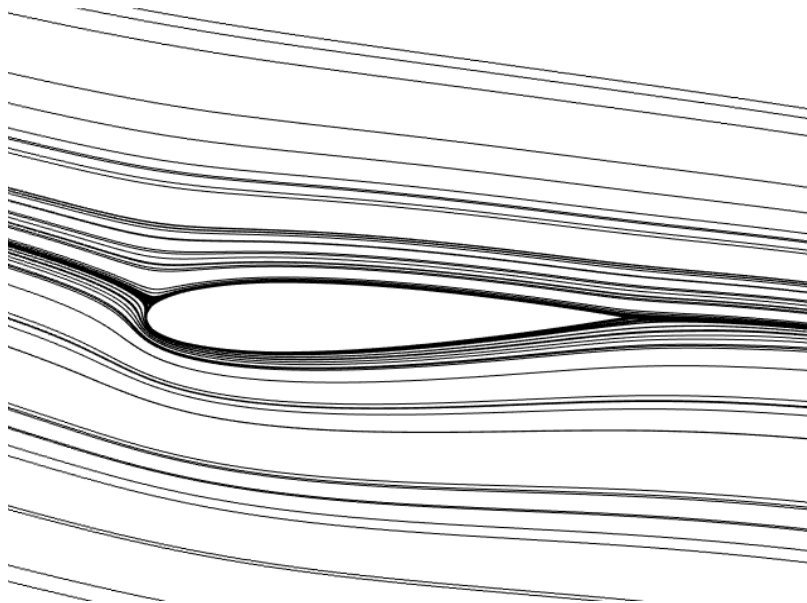
(a) $\alpha = 16^\circ$; $\omega = 18.67$ rad/s



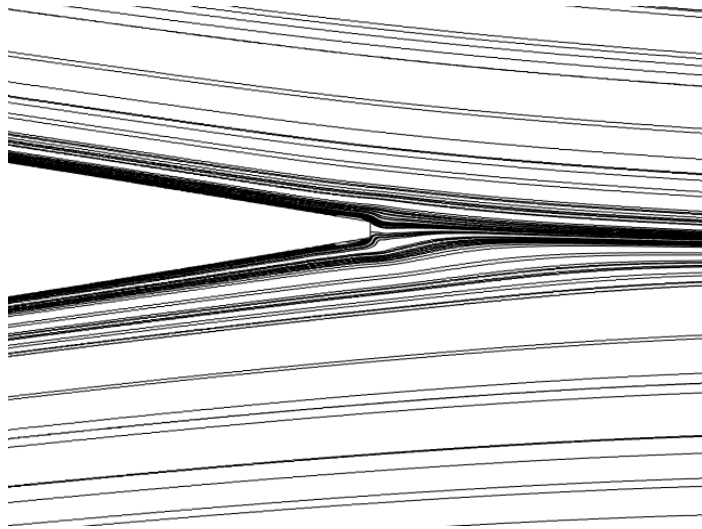
(b) $\alpha = 5^\circ$; $\omega = 18.67$ rad/s



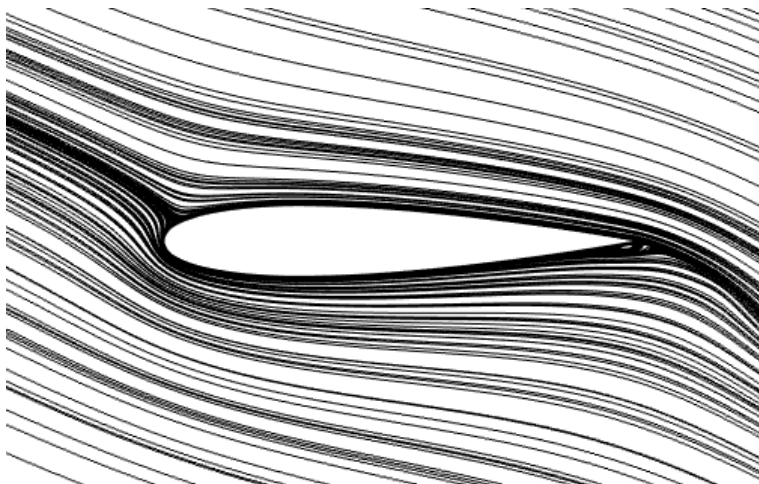
(c) $\alpha = -5^\circ$; $\omega = 18.67$ rad/s



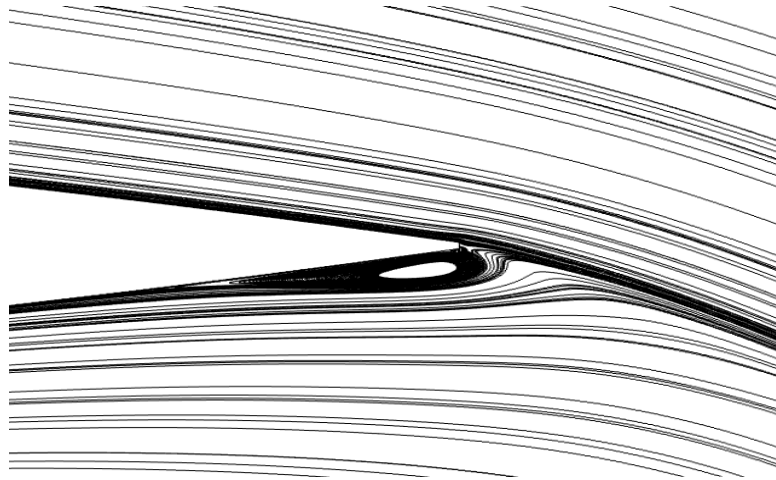
(d) $\alpha = -16.6^\circ$; $\omega = 18.67$ rad/s



(e) $\alpha = -16.6^\circ$; $\omega = 18.67$ rad/s (near the trailing edge)



(f) $\alpha = -16.6^\circ$; $\omega = 41.89$ rad/s



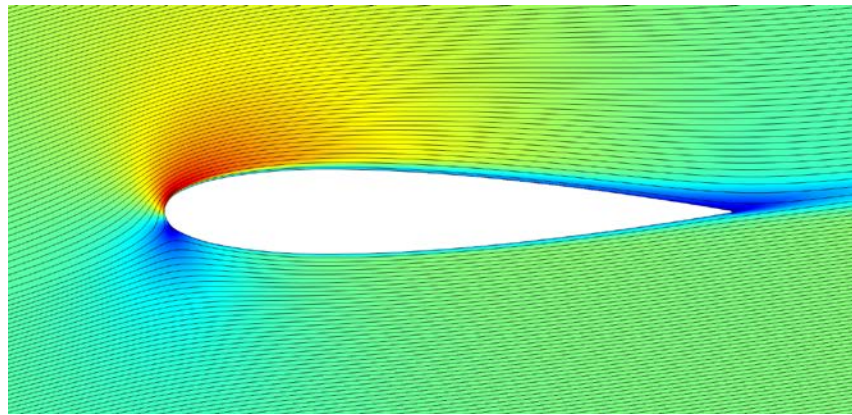
(g) $\alpha = -16.6^\circ$; $\omega = 41.89$ rad/s (flow recirculation near the trailing edge)

Figure 4.9. Streamlines around the aerofoil surface for the oscillating motion (a)-(e): $16.6^\circ \sin(18.67t)$ and (f)-(g): $16.6^\circ \sin(41.89t)$.

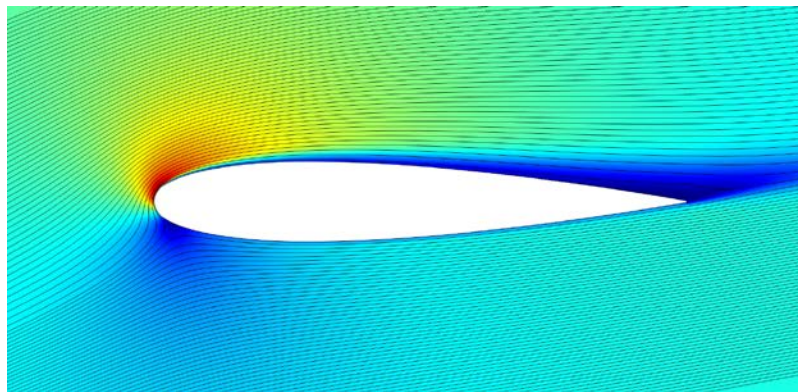
4.5. Performance comparison between the standard NACA 0015 and the optimized aerofoil

This section will describe the performance of the optimized aerofoil and compare the results with the regular NACA 0015 aerofoil. From the previous section, it is observed that the performance of the wind turbine is too much sensitive with the reduced frequency values even other parameters are kept constant. Hence, the results are compared only for the angular frequency 18.67 rad/s. At this angular speed good quasi-steady condition values has been obtained. The optimized blade performance is compared for two different oscillating motions: (a) $8^\circ + 10.6^\circ \sin(18.67t)$ and (b) $5^\circ + 16.6^\circ \sin(18.67t)$. In order to understand the instantaneous flow at different positions in the oscillation cycle and compare the results, Figure 4.10 is used to represent the velocity contours superimposed with flow streamlines at $Re_c = 3.6 \times 10^5$. From Figure 4.10, an almost attached flow is observed throughout the motion of the aerofoil. At a higher angle of attack (18°) small flow recirculation has been observed due to the fluid-structure interaction case for the rapid pitching of the aerofoil. It is also seen from Figure 4.10 (c) and (f) that optimized aerofoil exhibits a very little upper surface (suction side) flow recirculation or flow separation compared to the standard NACA 0015 aerofoil. As the upper surface flow recirculation is the cause of stall condition, this phenomenon should be avoided or needed to be delayed. Due to the optimized configuration of Gurney flap

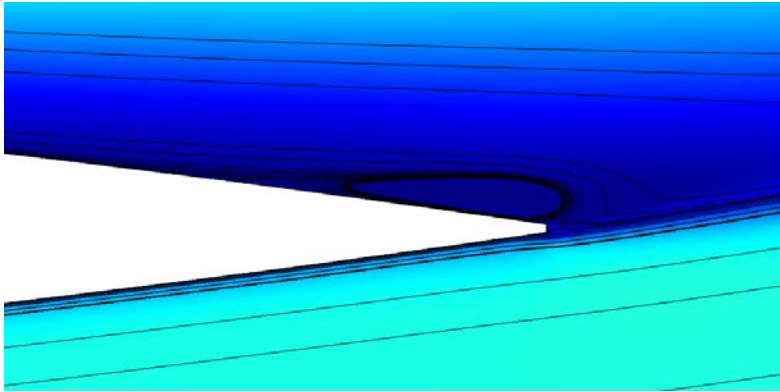
and dimple, the flow separation has been delayed and observed at $AOA > 18^\circ$ but for the standard NACA 0015 aerofoil case it has been observed approximately at $AOA > 15.5^\circ$. Thus, the optimized aerofoil shows better results. Figure 4.11 and Figure 4.12 plot the tangential force over five oscillations for two different chordal Reynolds numbers. It is seen from these figures that five cycles provide sufficient time to achieve a quasi-steady state condition. The figures also indicate that the optimized aerofoil achieves improved aerodynamic performance. The performances of the optimized blades are also tested for double blades condition.



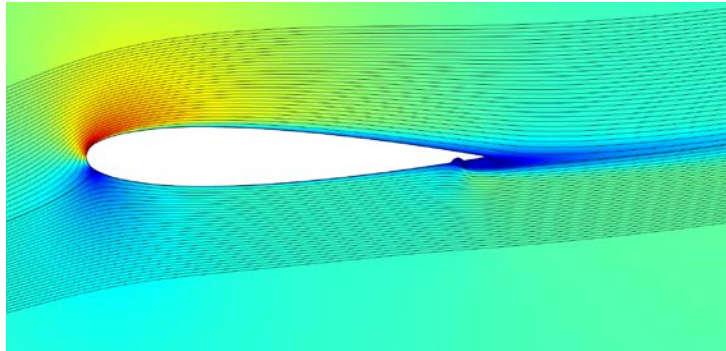
(a) $\alpha = 8^\circ$; NACA 0015 aerofoil



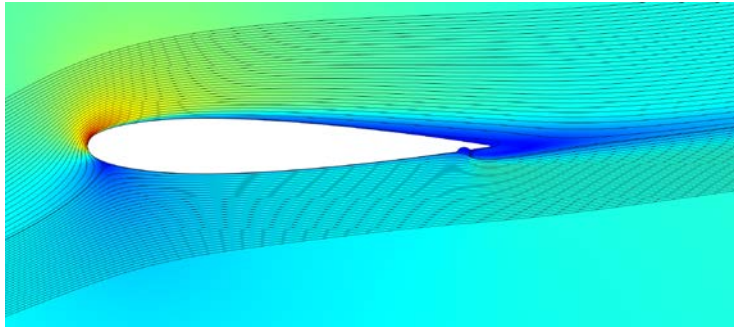
(b) $\alpha = 18.6^\circ$; NACA 0015 aerofoil



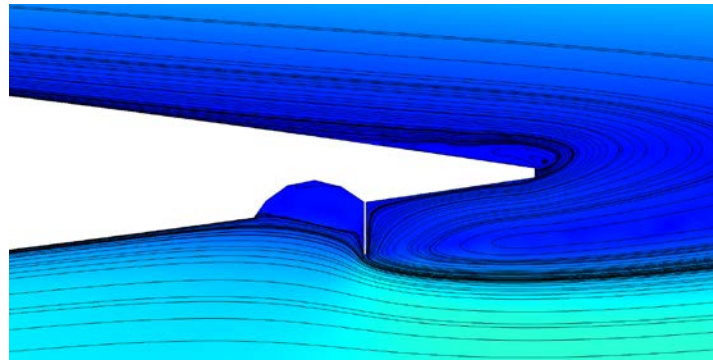
(c) $\alpha = 18.6^\circ$; NACA 0015 aerofoil (near the trailing edge)



(d) $\alpha = 8^\circ$; Optimized aerofoil



(e) $\alpha = 18.6^\circ$; Optimized aerofoil



(f) $\alpha = 18.6^\circ$; Optimized aerofoil (near the trailing edge)

Velocity (m/s)



Figure 4.10. Velocity contours (single blade) superimposed with the streamlines for for the oscillating motion $8^\circ + 10.6^\circ \sin(18.67t)$ at different angles of attack at $Re_c = 3.6 \times 10^5$: (a)-(c) NACA 0015 and (d)-(f) optimized aerofoil.

Figure 4.13 shows the velocity contours (double blades) for the oscillating motion $5^\circ + 16.6^\circ \sin(18.67t)$ at $Re_c = 2.35 \times 10^5$. It is observed that due to the optimized configuration of gurney flap and dimple, the velocity at the lower surface (pressure side surface) of the aerofoil is lower than the standard NACA 0015 aerofoil. This indicates the higher pressure at the lower side or the pressure side surface of the aerofoil which in turn can increase the tangential force of the aerofoil. Figure 4.14 to Figure 4.16 show the performance of the optimized aerofoil for single and double blade cases at different oscillating conditions.

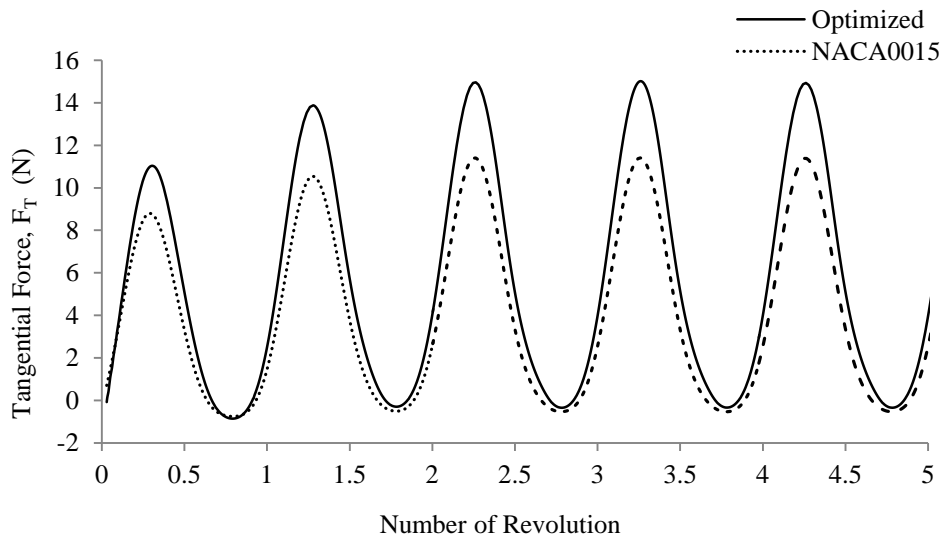


Figure 4.11. Tangential force comparison (single blade) between NACA 0015 and optimized aerofoil at $Re_c = 3.6 \times 10^5$ for oscillating motion: $8^0 + 10.6^0 \sin(18.67t)$.

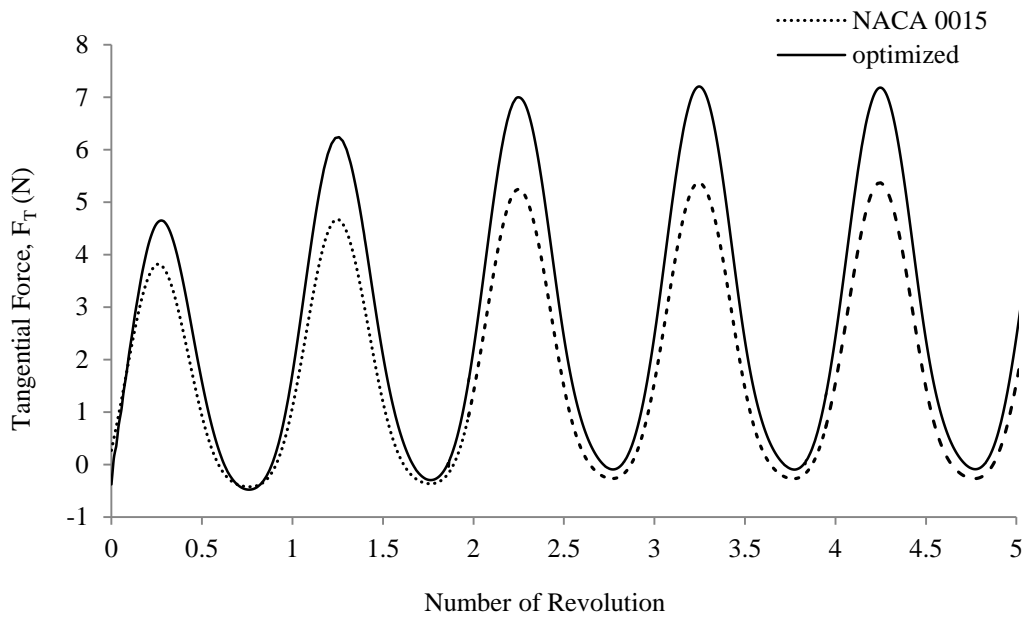
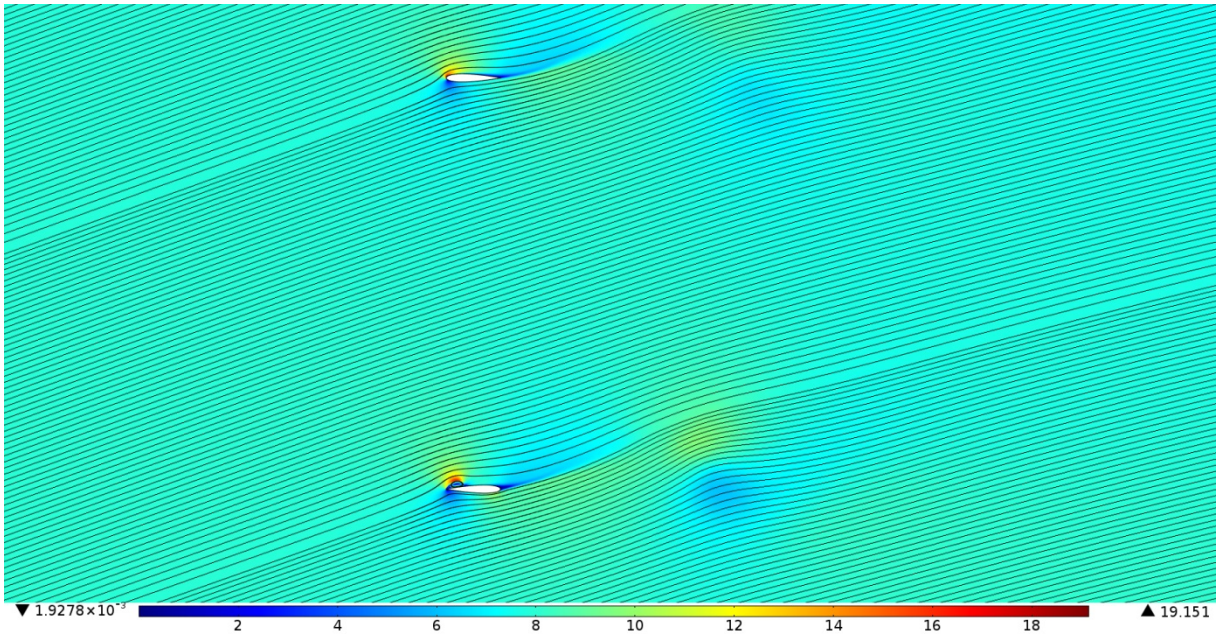
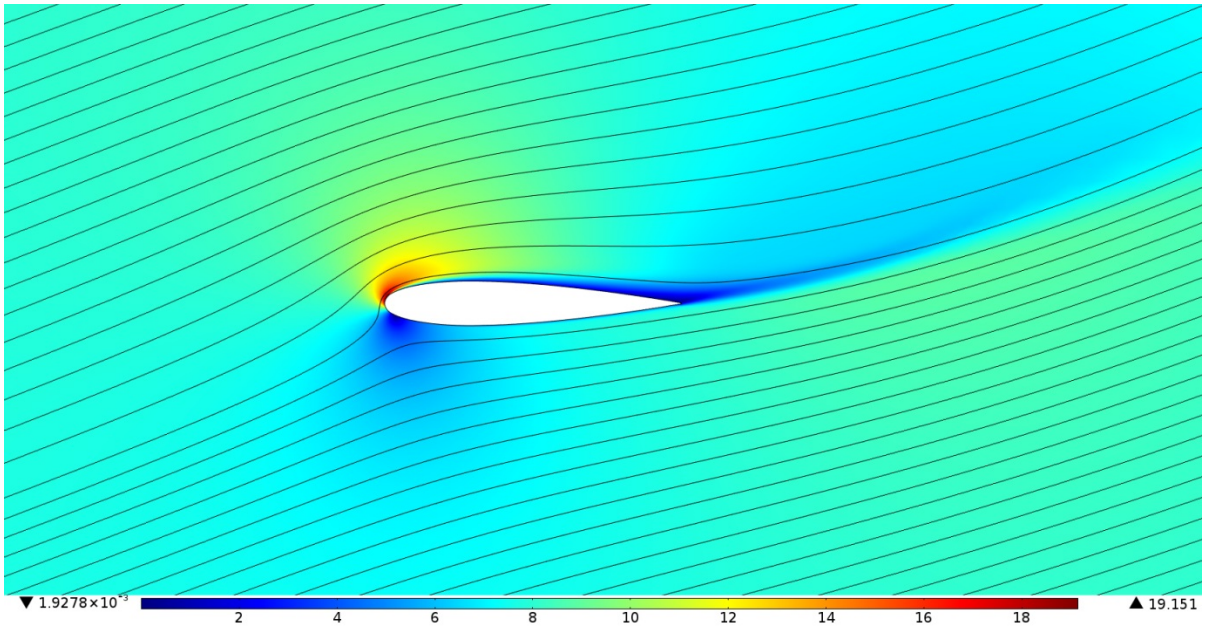


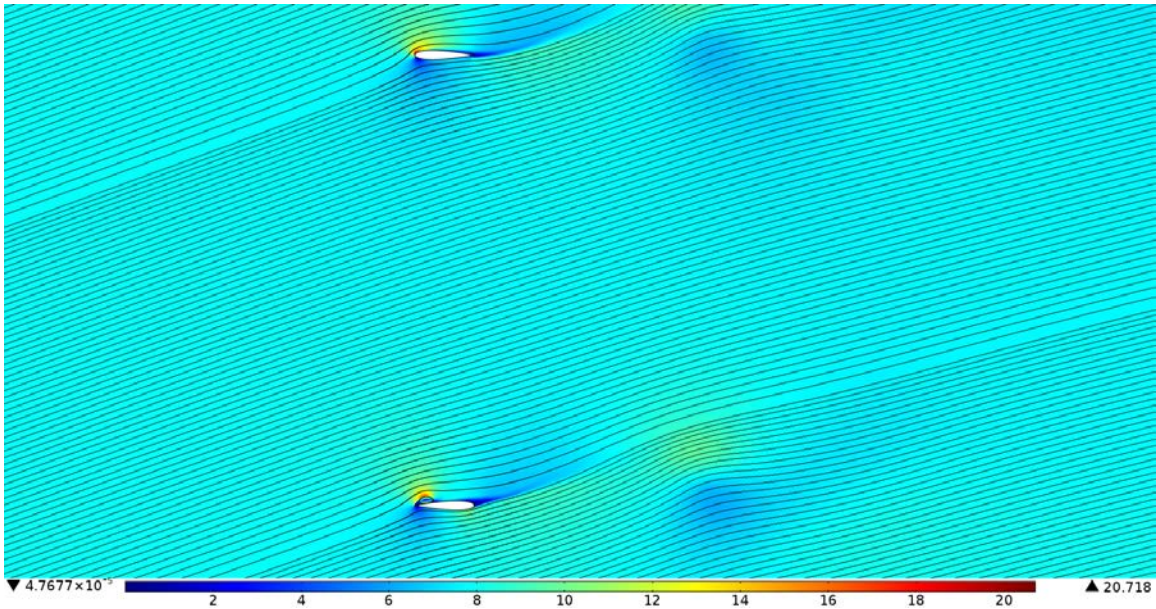
Figure 4.12. Tangential force comparison (single blade) between NACA 0015 and optimized aerofoil at $Re_c = 2.35 \times 10^5$ for oscillating motion: $8^0 + 10.6^0 \sin(18.67t)$.



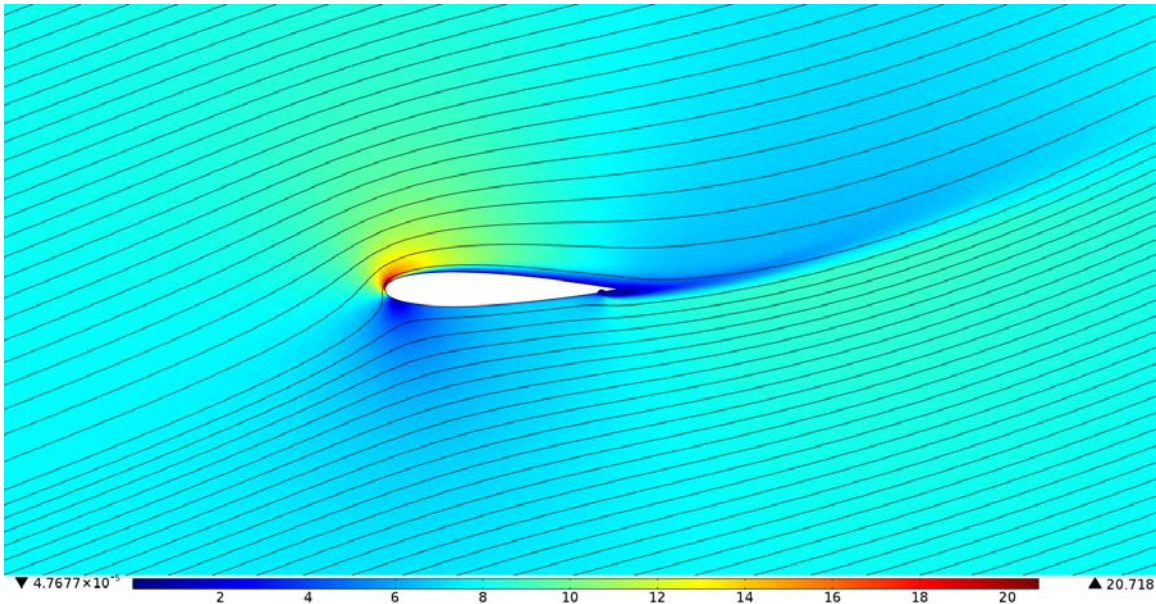
(a) $\alpha = 21.6^\circ$; NACA 0015 aerofoil



(b) $\alpha = 21.6^\circ$; NACA 0015 aerofoil (close view)



(c) $\alpha = 21.6^\circ$; optimized aerofoil



(d) $\alpha = 21.6^\circ$; optimized aerofoil (close view)

Figure 4.13. Velocity contours (m/s) superimposed with the streamlines for the oscillating motion $5^\circ + 16.6^\circ \sin(18.67t)$ at $Re_c = 2.35 \times 10^5$: (a)-(b) NACA 0015 and (c)-(d) optimized aerofoil (double blade).

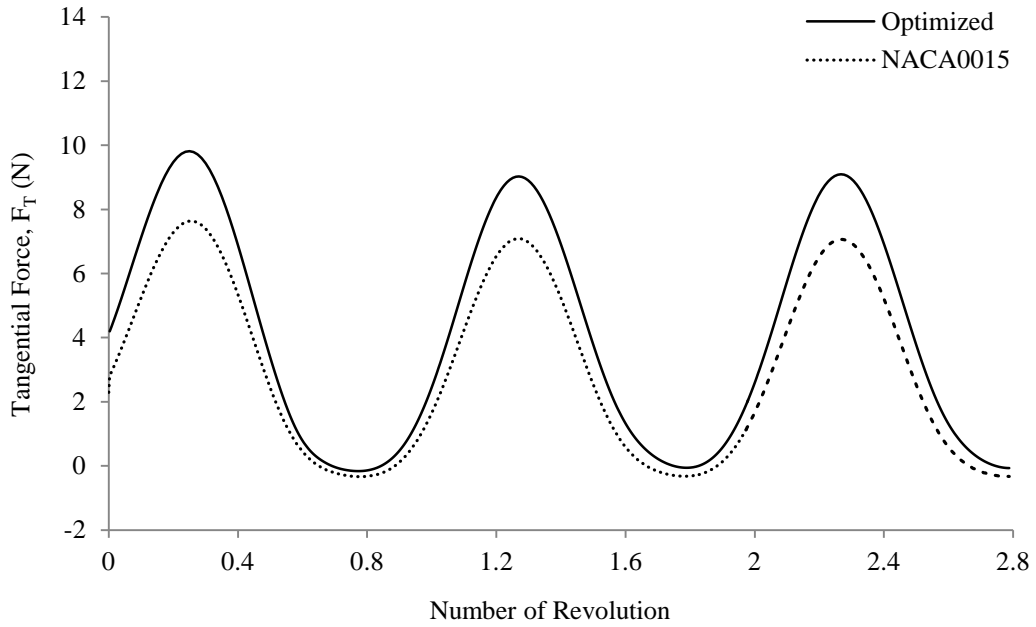


Figure 4.14. Tangential force comparison (double blade) between NACA 0015 and optimized aerofoil at $Re_c = 2.35 \times 10^5$ for oscillating motion: $8^0 + 10.6^0 \sin(18.67t)$.

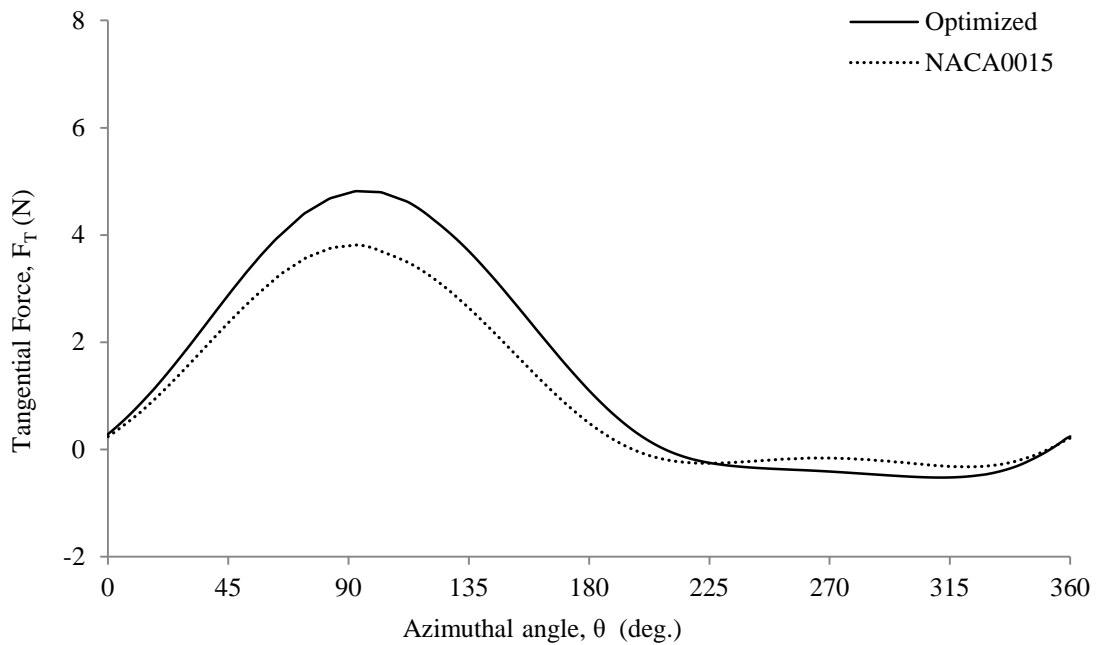


Figure 4.15. Tangential force comparison (single blade) between NACA 0015 and optimized aerofoil at $Re_c = 2.35 \times 10^5$ for oscillating motion: $5^0 + 16.6^0 \sin(18.67t)$.

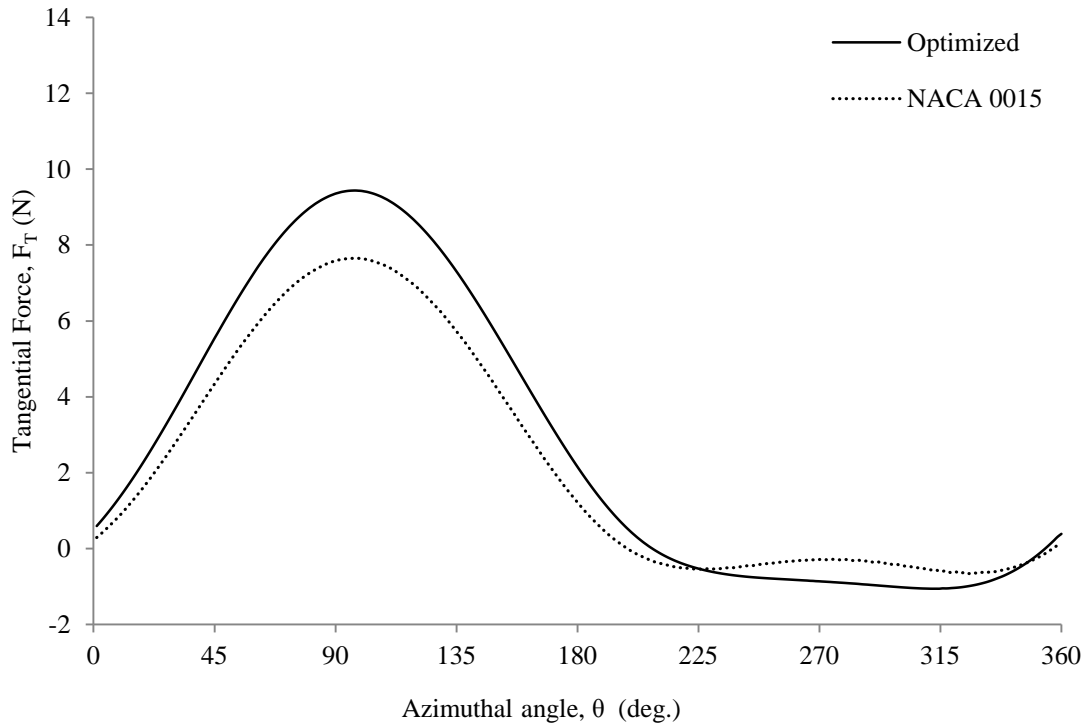


Figure 4.16. Tangential force comparison (double blade) between NACA 0015 and optimized aerofoil at $Re_c = 2.35 \times 10^5$ for oscillating motion: $5^0 + 16.6^0 \sin(18.67t)$.

The overall performance increment are shown in Table 4.1 for different oscillating flow conditions at $Re_c = 2.35 \times 10^5$. The table indicates that optimized aerofoil has the higher tangential force values than the standard NACA 0015 aerofoil and it shows better performance increment if the VAWT blade will be operated before deep dynamic stall conditions ($AOA < 20^0$). The tangential force values for the oscillating motion $5^0 + 16.6^0 \sin(18.67t)$ can be expressed as the function of azimuthal angle (θ) using the following equation at $Re_c = 2.35 \times 10^5$ (single blade case):

$$F_t = a_1 \times \sin(b_1 \times \theta + c_1) + a_2 \times \sin(b_2 \times \theta + c_2) + a_3 \times \sin(b_3 \times \theta + c_3) + a_4 \times \sin(b_4 \times \theta + c_4) \quad (4.5)$$

Here, the values of the constants for standard NACA 0015 aerofoil are:

$a_1 = 2.588$; $b_1 = 0.0009902$; $c_1 = 0.2587$; $a_2 = 0.7236$; $b_2 = 0.0348$; $c_2 = -1.667$; $a_3 = 2.189$; $b_3 = 0.01643$; $c_3 = 0.1271$; $a_4 = 0.01892$; $b_4 = 0.07579$; $c_4 = -3.835$.

and the values of the constants for the optimized aerofoil are:

$a_1 = 3.58$; $b_1 = 0.0009837$; $c_1 = 0.2319$; $a_2 = 0.7554$; $b_2 = 0.03485$; $c_2 = -1.808$; $a_3 = 2.921$; $b_3 = 0.01635$; $c_3 = 0.05931$; $a_4 = -0.02224$; $b_4 = 0.07352$; $c_4 = -0.5506$.

Table 4.1 Performance comparison between NACA 0015 and optimized aerofoil

No. of Blades	Oscillating motion	Torque (N-m)		Performance increased (%)
		NACA 0015	Optimized	
1	$8^\circ + 10.6^\circ \sin(18.67t)$	2.06	2.86	39.0%
	$5^\circ + 16.6^\circ \sin(18.67t)$	1.65	2.16	30.9%
2	$8^\circ + 10.6^\circ \sin(18.67t)$	4.12	5.72	39.0%
	$5^\circ + 16.6^\circ \sin(18.67t)$	3.31	4.19	26.6%

Chapter 5.

Conclusions and Future Work

This study has proposed a RSA-based automated method to maximize the performance of VAWT blades by optimizing the configuration of a Gurney flap with an inward dimple. The algorithm can automatically change the RSA model by changing the DOE data set if deemed necessary. In this thesis, CFD simulations were used to obtain the data needed for the RSA optimization at low Reynolds number, $Re_c \sim 2.35 \times 10^5$ and a tip speed ratio of 3.5. The turbulence models used in the CFD study were valid against previously published experiments. From the study, it can be concluded that the maximum possible average tangential force can be increased by approximately 35% in steady state case and 40% in oscillating case (at each revolution for dynamic stall cases) by utilizing an optimized combination of Gurney flap and semi-circular inward dimple. The performance increment is larger for the dynamic case because there is a delay of flow separation for dynamic cases compared with the static one.

A few numerical works were carried out to investigate the tangential force variation for the dynamic pitching oscillation case. To the author's knowledge, this is the first time that such aerofoil modification effects have been studied for pitching oscillation condition at light dynamic stall condition. In this study, the tangential force variations were presented for both aerofoil cases: NACA 0015 and modified (optimized) one. Optimization under pitching oscillation condition at both light and deep dynamic stall cases is highly challenging problem to solve in terms of the computational resources, times, accuracy and appropriate turbulence model. Predicted tangential force values are also too much sensitive and being fluctuated with the angular frequency values for dynamic condition cases. This is also another reason to optimize the aerofoil parameters under steady state static conditions. Thus, the obtained optimized aerofoil can be applicable at any angular oscillating motion for the specific tip speed ratio value of 3.5.

The research of the current study can be extended in several directions. The optimization technique can also be checked for different tip speed ratio cases as well as different oscillating motion to make the modification effects more significant for vertical axis wind turbine application.

References

- [1] M. Balat, "A Review of Modern Wind Turbine Technology," *Energy Sources, Part A: Recovery, Utilization, and Environmental Effects*, vol. 31, no. 17. pp. 1561–1572, 2009.
- [2] McLaren Kevin W., "A numerical and experimental study of unsteady loading of high solidity vertical axis wind turbines," McMaster University, 2011.
- [3] M. Islam, D. S. K. Ting, and A. Fartaj, "Aerodynamic models for Darrieus-type straight-bladed vertical axis wind turbines," *Renewable and Sustainable Energy Reviews*, vol. 12, no. 4. pp. 1087–1109, 2008.
- [4] Lamma Winds, "http://en.wikipedia.org/wiki/Wind_turbine," *Wikipedia- The free encyclopedia*, . 2008.
- [5] Grobe H., "http://commons.wikimedia.org/wiki/File:Windgenerator_antarktis_hg.jpg," *Wikimedia Commons, the free media repository*. 2007.
- [6] C. P. van Dam, "Blade Aerodynamics- Passive and Active Load Control for Wind Turbine Passive and Active Load Control for Wind Turbine Blades," 2009.
- [7] Y. D. V. P. van Dam CP, "Gurney flap experiments of airfoil and wings," *J. Aircr.*, vol. 36, no. 2, pp. 484–486, 1999.
- [8] Winnemöller T. and C. P. Van Dam., "Design and Numerical Optimization of Thick Airfoils Including Blunt Trailing Edges," *J. Aircr.*, vol. 44.1, 2007.
- [9] R. E. Sheldahl and P. C. Klimas, "Aerodynamic characteristics of seven symmetrical airfoil sections through 180-degree angle of attack for use in aerodynamic analysis of vertical axis wind turbines," 1981.
- [10] O. Guerri, A. Sakout, and K. Bouhadeh, "Simulations of the Fluid Flow around a rotating Vertical Axis Wind Turbine," *Wind Eng.*, vol. 31, no. 3, pp. 149–163, 2007.
- [11] CFD Online, "http://www.cfd-online.com/Wiki/RANS-based_turbulence_models."

- [12] C. J. S. Ferreira, H. Bijl, G. van Bussel, and G. van Kuik, "Simulating Dynamic Stall in a 2D VAWT: Modeling strategy, verification and validation with Particle Image Velocimetry data," *Journal of Physics: Conference Series*, vol. 75. p. 012023, 2007.
- [13] C. J. Simão Ferreira, A. Van Zuijlen, H. Bijl, G. Van Bussel, and G. Van Kuik, "Simulating dynamic stall in a two-dimensional vertical-axis wind turbine: Verification and validation with particle image velocimetry data," *Wind Energy*, vol. 13, no. 1, pp. 1–17, 2010.
- [14] Turbulence modeling, http://www.cfd-online.com/Wiki/Turbulence_modeling. .
- [15] S. A. Ahmadi, S. Sharif, and R. Jamshidi, "A Numerical Investigation on the Dynamic Stall of a Wind Turbine Section Using Different Turbulent Models," in *WASET*, 2009, pp. 290–296.
- [16] K. Gharali and D. A. Johnson, "Numerical modeling of an S809 airfoil under dynamic stall, erosion and high reduced frequencies," *Appl. Energy*, vol. 93, pp. 45–52, 2012.
- [17] A. Fiedler, "The effects of blade pitch and mount point offset on vertical axis wind turbine performance," McMaster University, 2009.
- [18] Shengyi Wang, Lin Ma, Derek B Ingham, Mohamed Pourkashanian, and Zhi Tao, "Turbulence Modelling of Deep Dynamic Stall at Low Reynolds Number," in *World Congress on Engineering, Vol II, London, U.K.*, 2010.
- [19] H. Sun, "Wind turbine aerofoil design using response surface method," *J. Mech. Sci. Technol.*, vol. 25.5, pp. 1335–1340, 2011.
- [20] H. Sun and S. Lee, "Response surface approach to aerodynamic optimization design of helicopter rotor blade," *Int. J. Numer. Methods Eng.*, vol. 64, no. 1, pp. 125–142, 2005.
- [21] K. Hamada, T. Smith, N. Durrani, and R. J. Howell, "Unsteady flow simulation and dynamic stall around vertical axis wind turbine blades," in *46th AIAA Aerospace Sciences Meeting and Exhibit*, 2008, no. AIAA-2008–1319.
- [22] S. Wang, D. B. Ingham, L. Ma, M. Pourkashanian, and Z. Tao, "Numerical investigations on dynamic stall of low Reynolds number flow around oscillating airfoils," *Computers & Fluids*, vol. 39, no. 9. pp. 1529–1541, 2010.
- [23] T. LEE and P. GERONTAKOS, "Investigation of flow over an oscillating airfoil," *Journal of Fluid Mechanics*, vol. 512. 2004.
- [24] "COMSOL, 4.3 b. CFD module User's Guide," New England Executive Park, Burlington, Mass, USA,, 2013.

- [25] D. R. Troolin, E. K. Longmire, and W. T. Lai, "Time resolved PIV analysis of flow over a NACA 0015 airfoil with Gurney flap," in *Experiments in Fluids*, 2006, vol. 41, no. 2, pp. 241–254.
- [26] R. H. Liebeck, "Design of subsonic Airfoils for High Lift," *J. Aircr.*, vol. 15, pp. 547–561, 1978.
- [27] P. O. Neuhart DH, "A water tunnel study of Gurney flaps," 1988.
- [28] Myose R, Heron I, and Papadakis M, "Effect of Gurney Flaps on a NACA 0011 Aerofoil," *AIAA Pap.*, vol. 59, pp. 15–18, 1996.
- [29] Giguere P., Lemay J, and Dumas G, "Gurney flap effects and scaling for low-speed aerofoils," *AIAA Pap.*, vol. 95, p. 1881, 1995.
- [30] D. L. Katz J., "Study of an open-wheel racing car's rear-wing aerodynamics," *SAE Tech. Pap.*, no. 890600, 1989.
- [31] J. . L. R. Katz, "Effect of 90 degree flap on the aerodynamics of a two-element airfoil," *J. Fluids Eng.*, vol. 111.1, pp. 93–94, 1989.
- [32] van D. C. H. B. Vijgen PMHW, "Wind tunnel investigations of wings with serrated sharp trailing edges," in *Proceedings of the conference on low Reynolds number airfoil aerodynamics*, 1989, pp. 295–313.
- [33] Y. C. . Li, J. J. Wang, and P. F. Zhang, "Experimental Investigation of Lift Enhancement on a NACA0012 Airfoil Using Plate/Serrated Gurney Flaps," *ACTA Aeronaut. Astronaut. Sin. A B*, vol. 24, no. 2, pp. 119–123, 2003.
- [34] J. Y. . Li, R. . Li, Y. . Gao, and J. Huang, "Aerodynamic optimization of wind turbine aerofoils using response surface techniques," *Proc. Inst. Mech. Eng. Part A J. Power Energy*, vol. 224(6), 2010.
- [35] P. O. . Neuhart D.H, "A water tunnel study of Gurney flaps," 1988.
- [36] T. Lee, "Aerodynamic Characteristics of airfoil with Perforated Gurney-Type Flaps," *J. Aircr.*, vol. 46, no. 2, pp. 542–548, 2009.
- [37] Y. Li, Jinjun Wang, and Panfeng Zhang, "Effect of Gurney flaps on a NACA0012 airfoil," *Flow, Turbul. Combust.*, vol. 68.1, pp. 27–39, 2002.
- [38] L. W. . Traub and A. Akerson, "Airfoil Lift Augmentation at Low Reynolds Number," *J. Aircr.*, vol. 47, no. 6, pp. 2103–2114, 2010.

- [39] R. Myose, M. Papadakis, and I. Heron, "Gurney Flap Experiments on Airfoils, Wings, and Reflection Plane Model," *Journal of Aircraft*, vol. 35, no. 2. pp. 206–211, 1998.
- [40] S. L. Gai and R. Palfrey, "Influence of trailing-edge flow control on airfoil performance," *J. Aircr.*, vol. 40.2, pp. 332–337, 2003.
- [41] G. S. Dulikravich, "Aerodynamic shape design and optimization: status and trends," *J. Aircr.*, vol. 29.6, pp. 1020–1026, 1992.
- [42] P. K. N. Srivastav Deepanshu, "Surface modifications for improved maneuverability and performance of an aircraft," in *ASME 2011 International Mechanical Engineering Congress and Exposition*, 2011, pp. 121–127.
- [43] M. S. N. H. J. R. Mirzaei, "Single and multi-point optimization of an airfoil using gradient method," *Aircr. Eng. Aerosp. Technol.*, vol. 79.6, pp. 611–620, 2007.
- [44] A. . Q. Vavalle, "Interactive response surface based optimization scheme for transonic airfoil design," *J. Aircr.*, vol. 44, pp. 365–376, 2007.
- [45] R. H. Myers and C. M. Anderson-Cook, *Response Surface Methodology: Process and Product Optimization Using Designed Experiments.*, 705th ed. John Wiley & Sons, 2009.
- [46] F. Factor and Experiment Design Matrix, "Response Surface Modeling of Combined-Cycle Propulsion Components Using Computational Fluid Dynamics," in *40th Aerospace Sciences Meeting and Exhibit*, 2002.
- [47] N. R. Draper, "Response surface methodology: Process and product optimization using designed experiments," *Journal of Statistical Planning and Inference*, vol. 59, no. 1. pp. 185–186, 1997.
- [48] A. A. Giunta, *Aircraft multidisciplinary design optimization using design of experiments theory and response surface modeling methods*, no. May. 1997.
- [49] B. Ozcelik and T. Erzurumlu, "Determination of effecting dimensional parameters on warpage of thin shell plastic parts using integrated response surface method and genetic algorithm," *Int. Commun. Heat Mass Transf.*, vol. 32, no. 8, pp. 1085–1094, 2005.
- [50] A. I. Forrester, N. W. Bressloff, and A. J. Keane., "Optimization using response surface models and partially converged computational fluid dynamics simulations," *Proc. R. Soc. A Math. Phys. Eng. Sci.*, vol. 462.2071, pp. 2177–2204, 2006.
- [51] J. I. Madsen, W. Shyy, and R. T. Haftka, "Response surface techniques for diffuser shape optimization," *AIAA Journal*, vol. 38. pp. 1512–1518, 2000.

- [52] K. . C. L. . M. W. McAlister, "Dynamic Stall Experiments on the NACA0012 Airfoil," 1978.
- [53] W. McCroskey, "Unsteady airfoils," *Annu. Rev. Fluid Mech.*, vol. 14, pp. 285–311, 1982.
- [54] Piziali, "An Experimental Investigation of 2D end 3D Oscillating Wing Aerodynamics for a Range of Angle of Attack Including Stall," Ames, CA, 1993.
- [55] K. K. Y. . Tsang, R. M. C. . So, R. C. K. . Leung, and X. Q. Wang, "Dynamic stall behaviour from unsteady force measurements," *J. Fluid Struct.*, vol. 24, pp. 129–150, 2008.
- [56] F. Menter, "Zonal Two Equation k-w Turbulence Models for Aerodynamics Flows.," *AIAA Pap.* , vol. 93–2906, 1993.
- [57] F. R. Menter, "Two-equation eddy-viscosity turbulence models for engineering applications," *AIAA Journal*, vol. 32, no. 8. pp. 1598–1605, 1994.
- [58] D. C. Wilcox, *Turbulence Modeling for CFD (Second Edition)*. 1998.
- [59] Gerontakos Panayiot, "An experimental investigation of flow over an oscillating airfoil ," McGill University, Montreal, Quebec, Canada, 2004.
- [60] S. Wang, D. B. Ingham, L. Ma, M. Pourkashanian, and Z. Tao, "Turbulence modeling of deep dynamic stall at relatively low Reynolds number," *J. Fluids Struct.*, vol. 33, pp. 191–209, 2012.
- [61] K. M. . I. D. B. . M. L. . & P. M. Almohammadi, *Effect of Transitional Turbulence Modelling on a Straight Blade Vertical Axis Wind Turbine*. Alternative Energies. Springer Berlin Heidelberg, 2013, pp. 93–112.
- [62] F. . & J. I. Kanyako, *Numerical Investigation of Four Commonly Used Airfoils for Vertical Axis Wind Turbine*. CREGA'14-Renewable Energy: Generation and Applications, Springer International Publishing, 2014, pp. 443–454.
- [63] J. McNaughton, F. Billard, and A. Revell, "Turbulence modelling of low Reynolds number flow effects around a vertical axis turbine at a range of tip-speed ratios," *Journal of Fluids and Structures*, 2014.
- [64] L. A. Danao, N. Qin, and R. Howell, "A numerical study of blade thickness and camber effects on vertical axis wind turbines," *Proc. Inst. Mech. Eng. Part a- Journal Power Energy*, vol. 226, no. A7, pp. 867–881, 2012.
- [65] Douvi C. Eleni, "Evaluation of the turbulence models for the simulation of the flow over a National Advisory Committee for Aeronautics (NACA) 0012 airfoil," *Journal of Mechanical Engineering Research*, vol. 4, no. 3. 2012.

- [66] P. R. Spalart and S. R. Allmaras, "A one-equation turbulence model for aerodynamic flows," *La Rech. Aerosp.*, vol. 1, no. 1, pp. 5–21, 1994.
- [67] W. . Jones and B. . Launder, "The prediction of laminarization with a two-equation model of turbulence," *International Journal of Heat and Mass Transfer*, vol. 15, no. 2. pp. 301–314, 1972.
- [68] D. Thévenin and G. Janiga, *Optimization and Computational Fluid Dynamics*, vol. XVI. 2008, p. 294.
- [69] H. M. Kim and K. Y. Kim, "Design optimization of rib-roughened channel to enhance turbulent heat transfer," *Int. J. Heat Mass Transf.*, vol. 47, no. 23, pp. 5159–5168, 2004.
- [70] Mathworks, "Mathworks documentation Center."
- [71] O. . Dahou, K. . Medles, S. . Touhami, M. F. . Boukhoulda, A. . Tilmatine, and L. Dascalescu, "Application of genetic algorithms to the optimization of a roll-type electrostatic separation process," *Ind. Appl. IEEE Trans.* , vol. 47.5 , pp. 2218–2223, 2011.
- [72] D. E. Goldberg, *Genetic Algorithms in Search, Optimization, and Machine Learning*, vol. Addison-We. Addison-Wesley, 1989, p. 432.
- [73] MATLAB ANOVA, <http://www.mathworks.com/help/stats/analysis-of-variance-anova-1.html> .
- [74] Wikipedia, <http://en.wikipedia.org/wiki/P-value> .
- [75] Simulated Annealing, <http://www.mathworks.com/discovery/simulated-annealing.html> .
- [76] Ismail M.F. and Vijayaraghavan K., "Investigation of flow over an oscillating aerofoil for wind turbine application," in *Canadian Society for Mechanical Engineering (CSME) International Congress, Toronto, Canada*, 2014.
- [77] Ismail M. F. and Vijayaraghavan K., "CFD analysis of the effects of surface modification of a vertical axis wind turbine blade for improved aerodynamic flow control," in *12th Americas Conference on Wind Engineering, Seattle, Washington, USA* , 2013.
- [78] Ismail M.F. and Vijayaraghavan K., "The effects of aerofoil profile modification on a vertical axis wind turbine performance," *Energy, Elsevier Pub.(Under revis.)*, 2014.